

Lattice Boltzmann Methods for thermal flows: continuum limit and applications to compressible Rayleigh-Taylor systems.

A. Scagliarini,¹ L. Biferale,¹ M. Sbragaglia,² K. Sugiyama,³ and F. Toschi⁴

¹*Department of Physics and INFN, University of Tor Vergata,
Via della Ricerca Scientifica 1, 00133 Rome, Italy
and International Collaboration for Turbulence Research*

²*Department of Physics and INFN, University of Tor Vergata,
Via della Ricerca Scientifica 1, 00133 Rome, Italy*

³*Department of Mechanical Engineering, School of Engineering,
The University of Tokyo, 7-3-1, Hongo, Bunkyo-ku, Tokyo 113-8656, Japan*

⁴*Department of Physics and Department of Mathematics and Computer Science,
Eindhoven University of Technology, 5600 MB Eindhoven,
The Netherlands; and International Collaboration for Turbulence Research*

We compute the continuum thermo-hydrodynamical limit of a new formulation of lattice kinetic equations for thermal compressible flows, recently proposed in [Sbragaglia et al., *J. Fluid Mech.* **628** 299 (2009)]. We show that the hydrodynamical manifold is given by the correct compressible Fourier-Navier-Stokes equations for a perfect fluid. We validate the numerical algorithm by means of exact results for transition to convection in Rayleigh-Bénard compressible systems and against direct comparison with finite-difference schemes. The method is stable and reliable up to temperature jumps between top and bottom walls of the order of 50% the averaged bulk temperature. We use this method to study Rayleigh-Taylor instability for compressible stratified flows and we determine the growth of the mixing layer at changing Atwood numbers up to $At \sim 0.4$. We highlight the role played by the adiabatic gradient in stopping the mixing layer growth in presence of high stratification and we quantify the asymmetric growth rate for spikes and bubbles for two dimensional Rayleigh-Taylor systems with resolution up to $L_x \times L_z = 1664 \times 4400$ and with Rayleigh numbers up to $Ra \sim 2 \times 10^{10}$.

I. INTRODUCTION

Lattice implementations of discrete-velocity kinetic models have gained considerable interest in the last decades, as efficient tools for the theoretical and computational investigation of the physics of complex flows [1–8]. An important class of discrete-velocity models for ideal fluid flows, the lattice Boltzmann models (LBM) [9–11] can be derived from the continuum Boltzmann (BGK) equation [12], upon expansion in Hermite velocity space of the single particle distribution function, $f(\mathbf{x}, \boldsymbol{\xi}, t)$, describing the probability of finding a molecule at space-time location (\mathbf{x}, t) and with velocity $\boldsymbol{\xi}$ [4, 13–15]. As a result, the corresponding lattice dynamics acquires a systematic justification in terms of an underlying continuum kinetic theory. The state-of-the-art is satisfactory concerning iso-thermal flows, even in presence of complex bulk physics (multi-phase, multi-components) [1, 2, 16] and/or with complex boundary conditions such as roughness, non-wetting walls and slip-length [6, 17–19].

The situation is much less satisfactory when temperature plays an active role in the flow evolution, due to complex compressible effects which are present even in ideal fluid/gas or to phase-change in multi-phase systems, or both. Only a few years ago, one could frankly admit that not a single known Lattice Boltzmann approach could handle, in a realistic way, thermal problems properly. The main difficulties being the development of subtle instabilities when the local velocity increases. In the last years, the situation has started to improve, with different attempts being made to describe active thermal modes within a fully discretized Boltzmann approach [15, 20–28]. These studies show that in order to recover the right continuum descriptions with the correct symmetries for the internal energy flux, one needs to enlarge the number of discrete speeds (a possible choice, for space filling schemes following a Gauss-Hermite quadrature [15, 26], is 37 speeds in 2d [26, 29] and 107 speeds in 3d [30]), or to add ad-hoc counter-terms canceling spurious anisotropic operators [21, 22]. Otherwise, different hybrid attempts have been proposed, where temperature evolution is solved using finite difference methods [20] or with lattice schemes able to reproduce thermal Van der Waals fluids in the continuum limit [24]. Boundary conditions [23, 31] and stability issues [32] are also much more involved when thermal modes are present. It is fair to say that not a single model emerged as the optimal choice, and only a few explorative studies have been performed in order to check potentiality and limitations of each proposed solution.

The aim of this paper is twofold. First, we intend to further discuss a recent formulation, proposed by some of us in [33], for a new way to incorporate the effects of external/internal forces in thermal LBM. We provide here the full explicit Chapman-Enskog expansion, whose results were only anticipated without proof in [33], in order to show the convergence of the model to the Fourier-Navier-Stokes equations. We validate the method in a case where thermal

compressible effects play a major role, i.e. the transition to convection in a compressible Rayleigh-Bénard system of height L_z , with an imposed temperature jump, $T_u - T_d = \Delta T$. For such systems, it is possible to calculate the critical Rayleigh number analytically [34] at changing both the stratification parameter (also known as the scale height), $Z = \Delta T/T_u$, and the polytropic index, $m = g/(R\beta) - 1$, where R is the gas constant, g the gravity acceleration and $\beta = \Delta T/L_z$ the temperature gradient. We show here that our LBM scheme is able to handle temperature jumps as high as $\Delta T/T_u = 2$ for both positive and negative values of the polytropic index (stable and unstable density stratification). Such systems are clearly very far from the classical Oberbeck-Boussinesq approximation [35, 36].

Second, we study highly compressible Rayleigh-Taylor systems, for the initial configuration where two blobs of the same fluids are prepared with two different temperatures (hot, less dense, blob below, cold, denser, blob above). We show that the method is able to handle the highly non-trivial spatio-temporal evolution of the system even in the developing turbulent phase. In this case, we could push the numerics up to Atwood numbers $At \sim 0.4$. Maximum Rayleigh numbers achieved are $Ra \sim 4 \times 10^{10}$ for $At = 0.05$ and $Ra \sim 2 \times 10^9$ for $At = 0.4$. We present results on: (i) the growth of the mixing-layer at changing the compressibility degree, including the asymmetry in the quadratic growth of spikes and bubbles dynamics; (ii) a new effect of stratification which stops the mixing length growth when a critical width, L_{ad} is reached. We interpret this as due to the existence of the *adiabatic gradient*: when the jumps between the two moving fronts leads to a temperature gradient, $\Delta T/L_{ad}$, of the order of the *adiabatic gradient* the dynamics stops and only thermal diffusive mixing may further acts.

Technically speaking, the main novelty of the thermal-LBM formulation proposed in [33] relies on the fact that it is possible to incorporate the effects of an external and/or internal force (gravity and/or intermolecular potential) via a suitable shift of both momentum and temperature appearing in the local equilibrium distribution of the Boltzmann collision operator. Doing that, the systems acquires an elegant self-consistent formulation and a stable spatio-temporal evolution also in presence of compressible effects, as demonstrated by the examples anticipated before and detailed later.

The paper is organized as follows. In Section II we briefly remind the details of the LBM formulation and we discuss the first result of this paper: the continuum thermo-hydrodynamical limit, given by the Fourier-Navier-Stokes eqs., as obtained from a rigorous Chapman-Enskog expansion of the discrete model. In Section III we show first the validation of the discretized algorithm by studying the transition to convection in compressible Rayleigh-Bénard systems and comparing the results with exact analytical calculations, at changing the scale height and the polytropic index. In the same section we also present validation of the method against finite-difference methods, for the same set-up but after the transition, once convective rolls are present and stationary. In Section IV we show the investigations of another non-trivial compressible case: Rayleigh-Taylor system, for two different Atwood numbers $At = 0.05$ and $At = 0.4$. Conclusions and perspectives close the paper in Section V.

II. THERMAL KINETIC MODEL AND CONTINUUM THEORY

The main goal of this section is to show how to use a Thermal-LBM to discretize continuum thermal kinetic equations in presence of internal/external forces and how to extract via a suitable Chapman-Enskog multiscale expansion the relative hydrodynamical evolution, given in term of the *forced* Fourier-Navier-Stokes equations. The first issue was already discussed in [33]: here we briefly recall it and then discuss the second issue in details.

A Thermal-Kinetic description of a compressible gas/fluid of variable density, ρ , local velocity \mathbf{u} , internal energy, \mathcal{K} and subjected to a local body force density, \mathbf{g} , is given in the continuum by the following set of equations (repeated indices are summed upon):

$$\begin{cases} \partial_t \rho + \partial_i(\rho u_i) = 0 \\ \partial_t(\rho u_k) + \partial_i(P_{ik}) = \rho g_k \\ \partial_t \mathcal{K} + \frac{1}{2} \partial_i q_i = \rho g_i u_i \end{cases} \quad (1)$$

where P_{ik} and q_i are momentum and energy fluxes (still unknown at this level of description).

In [33], it is shown that it is possible to recover exactly the above set of equations, starting from a continuum Boltzmann Equations and introducing a suitable shift of the velocity and temperature fields entering in the local equilibrium: $f^{(eq)}(\boldsymbol{\xi}; \rho, T, \mathbf{u}) \rightarrow f^{(eq)}(\boldsymbol{\xi}; \rho, \bar{T}, \bar{\mathbf{u}})$. The new –shifted– Boltzmann formulation being:

$$\frac{\partial f}{\partial t} + \boldsymbol{\xi} \cdot \nabla f = -\frac{1}{\tau}(f - f^{(eq)}); \quad (2)$$

$$f^{(eq)}(\boldsymbol{\xi}; \rho, \bar{T}, \bar{\mathbf{u}}) = \frac{\rho}{(2\pi\bar{T})^{D/2}} e^{-|\boldsymbol{\xi} - \bar{\mathbf{u}}|^2/2\bar{T}}. \quad (3)$$

Where the shifted local velocity and temperature must take the following form:

$$\bar{\mathbf{u}} = \mathbf{u} + \tau \mathbf{g} \quad \bar{T} = T - \tau^2 g^2 / D. \quad (4)$$

The lattice counterpart of the continuum description (2) can be obtained through the usual lattice Boltzmann discretization:

$$f_l(\mathbf{x} + \mathbf{c}_l \Delta t, t + \Delta t) - f_l(\mathbf{x}, t) = -\frac{\Delta t}{\tau} (f_l(\mathbf{x}, t) - f_l^{(eq)})$$

where the equilibrium is expressed in terms of hydrodynamical fields on the lattice, $f_l^{(eq)}(\mathbf{x}, \rho^{(L)}, \bar{\mathbf{u}}^{(L)}, \bar{T}^{(L)})$, and the subscript l runs over the discrete set of velocities, \mathbf{c}_l . The superscript L indicates that the macroscopic fields are now defined in terms of the lattice Boltzmann populations:

$$\begin{cases} \rho^{(L)} = \sum_l f_l; \\ \rho^{(L)} \mathbf{u}^{(L)} = \sum_l \mathbf{c}_l f_l; \\ D \rho^{(L)} T^{(L)} = \sum_l |\mathbf{c}_l - \mathbf{u}^{(L)}|^2 f_l. \end{cases} \quad (5)$$

In [33] it was shown that the lattice version of the shifted fields entering in the Boltzmann equilibrium (see Appendix A for its detailed form) is:

$$\bar{\mathbf{u}}^{(L)} = \mathbf{u}^{(L)} + \tau \mathbf{g} \quad \bar{T}^{(L)} = T^{(L)} + \frac{\tau(\Delta t - \tau)g^2}{D} + \mathcal{O}(\Delta t)^2.$$

As it is known, lattice discretizations induce non trivial corrections terms in the macroscopic evolution of averaged hydrodynamical quantities. In particular both momentum and temperature must be renormalized by discretization effects in order to recover the correct thermal kinetic description (1) out of the discretized LBM variables. Density is left unchanged, $\rho^{(H)} = \rho$, while the first non trivial correction to momentum is given by the pre and post-collisional average [37, 38]:

$$\mathbf{u}^{(H)} = \mathbf{u}^{(L)} + \frac{\Delta t}{2} \mathbf{g} \quad (6)$$

and the first non-trivial, correction to the temperature field by [33]:

$$T^{(H)} = T^{(L)} + \frac{(\Delta t)^2 g^2}{4D}. \quad (7)$$

Using this *renormalized* hydrodynamical fields, one recover by a suitable Taylor expansions in Δt the thermo-hydrodynamical equations [33]:

$$\begin{cases} \partial_t \rho^{(H)} + \partial_i (\rho u_i^{(H)}) = 0 \\ \partial_t (\rho^{(H)} u_k^{(H)}) + \partial_i (P_{ik}^{(H)}) = \rho^{(H)} g_k \\ \partial_t \mathcal{K}^{(H)} + \frac{1}{2} \partial_i q_i^{(H)} = \rho^{(H)} g_i u_i^{(H)}. \end{cases} \quad (8)$$

The above equations are still unclosed. A closure ansatz to express the stress tensor, $P_{ik}^{(H)}$, and the heat flux, $q_i^{(H)}$, in terms of lower order moments is needed. This ends our short review of the backup material.

We proceed now with a systematic multi-scale closure of (8) in order to control the small wave-length limit where the full Fourier-Navier-Stokes equations emerge. The main added value with respect to previous similar calculations [40] is the explicit inclusion of the effects of the external force \mathbf{g} in the Chapman-Enskog expansion.

In order to perform the calculations, we need to introduce a hierarchy of temporal and spatial scales, via the introduction of a small parameter, ϵ :

$$\partial_t \rightarrow \epsilon \partial_{1t} + \epsilon^2 \partial_{2t}; \quad \partial_i \rightarrow \epsilon \partial_i$$

and the corresponding expansion for the Boltzmann distributions

$$f = f^{(0)} + \epsilon f^{(1)} + \epsilon^2 f^{(2)} + \epsilon^3 f^{(3)} + \epsilon^4 f^{(4)} + \dots$$

together with a suitable rescaling of the forcing terms, $g \sim \mathcal{O}(\epsilon)$ [37]. The various rescalings immediately reflect in the explicit expansion of the equilibrium distribution in terms of Hermite polynomials, $\mathcal{H}_l^{(n)}$:

$$f_l^{(eq)} = w_l \sum_n \frac{1}{n!} \mathbf{a}_0^{(n)} \mathcal{H}_l^{(n)}$$

where w_l are suitable weights [27, 29]. The projections on the different Hermite polynomials, $\mathbf{a}_0^{(n)}$, are explicitly given in Appendix A.

After a long calculation, fully detailed in the Appendix, one shows that the leading long wavelength limit coincides with the continuum Fourier-Navier-Stokes equations of an ideal compressible gas given by:

$$\begin{cases} \partial_t \rho + \partial_i(\rho u_i^{(H)}) = 0 \\ \rho \partial_t u_j^{(H)} + \rho u_i^{(H)} \partial_i u_j^{(H)} = \rho g_j + \partial_i \sigma_{ij}^{(H)} \\ \rho \partial_t e^{(H)} + \rho u_i^{(H)} \partial_i e^{(H)} = \sigma_{ij}^{(H)} \partial_j u_i^{(H)} + \partial_i (k \partial_i e^{(H)}); \end{cases} \quad (9)$$

with the ideal gas internal energy given by: $e^{(H)} = \frac{D}{2} T^{(H)}$. The stress tensor is given by:

$$\sigma_{ij}^{(H)} = -\rho T^{(H)} \delta_{ij} + \nu (\partial_i u_j^{(H)} + \partial_j u_i^{(H)}) + \delta_{ij} \left(\xi - \frac{\nu}{c_v} \right) \partial_k u_k^{(H)}.$$

The shear and bulk viscosities are:

$$\nu = T^{(H)} \rho \left(\tau - \frac{\Delta t}{2} \right); \quad \left(\xi - \frac{\nu}{c_v} \right) = -\frac{T^{(H)} \rho}{c_v} \left(\tau - \frac{\Delta t}{2} \right)$$

and the thermal conductivity:

$$k = c_p T^{(H)} \rho \left(\tau - \frac{\Delta t}{2} \right). \quad (10)$$

These are therefore the equations for a compressible gas with an ideal equation of state:

$$p = \rho T^{(H)} \quad (11)$$

and ideal specific heats:

$$c_v = \frac{D}{2}; \quad c_p = \frac{D}{2} + 1 \quad (12)$$

It is not difficult to show that in the case the external forces are conservative, written in a potential form depending only on the density, one may easily incorporate these effects in the definition of an internal energy, opening the way to discuss also non-ideal equations of state [33].

III. TRANSITION TO CONVECTION IN RAYLEIGH-BÉNARD COMPRESSIBLE SYSTEMS

A first non trivial application of the above algorithm can be found studying the behavior of Rayleigh-Bénard cells both considering the effects of compressibility and stratification to the transition from diffusive to convective dynamics [34, 41, 42] or to the case of fully turbulent non-Oberbeck-Boussinesq convection [36]. Here we concentrate on the first issue (see top panel of figure 1 for a schematic view), results on high Rayleigh turbulent convection will be published elsewhere. First, let us rewrite the set of equations (9) in a more transparent way, dropping for simplicity the superscript H in all variables and using the explicit expression of the internal energy in term of the temperature field:

$$\begin{cases} D_t \rho = -\rho \partial_i u_i \\ \rho D_t u_i = -\partial_i p - \rho g \delta_{i,z} + \eta \partial_{jj} u_i + \left(1 - \frac{1}{c_v} \right) \eta \partial_i \partial_j u_j \\ \rho c_v D_t T + p \partial_i u_i = k \partial_{ii} T + \eta (\partial_i u_j + \partial_j u_i - \frac{1}{c_v} \delta_{ij} \partial_k u_k) \partial_i u_j \end{cases} \quad (13)$$

where we have introduced the material derivative, $D_t = \partial_t + u_j \partial_j$, and we have assumed constant viscous and thermal conductivity coefficients [34, 43]. The equation of state is, $p = \rho T$, i.e. it is given in terms of quantities normalized such

that the gas constant is $R = 1$. For a cell of height L_z and with imposed bottom and top temperature, T_d and T_u , the hydrostatic equilibrium is easily found in terms of the temperature jump across the cell, $\beta = (T_d - T_u)/L_z = \Delta T/L_z$:

$$\begin{cases} T_0(z) = (T_d + T_u)/2 - \beta z \\ \rho_0(z) = \tilde{\rho} (T_0(z)/\tilde{T})^m \\ p_0(z) = \tilde{p} (T_0(z)/\tilde{T})^{m+1} \end{cases} \quad (14)$$

where the two integration constants must satisfy, $\tilde{p} = \tilde{\rho}\tilde{T}$, with \tilde{T} a reference temperature, $\tilde{T} = (T_u + T_d)/2$. In (14) we have introduced also the polytropic index: $m = g/\beta - 1$. At changing the polytropic index, one changes the hydrostatic profiles of density and pressure. In order to be unstable, the profile must obviously verify, $\beta > 0$ (if $g > 0$, as assumed here) and therefore the interesting polytropic interval is limited to $m \geq -1$. Furthermore, unstable fluctuations may develop only if the hydrostatic temperature gradient, β is larger than the *adiabatic gradient*, $\beta_{ad} = g/c_p$, i.e. only when the adiabatic transformation of a hot/cold spot of fluid moving up/down induces a temperature variation that does not exceed the hydrostatic change [44]. This limits the interesting interval excursion of the polytropic index from above, $m < c_p - 1$, which in our units, for an ideal gas in 2d, means $m < 1$. The limitation from above is a typical important example induced by compressibility/stratification, i.e. by the fact that a cold/hot fluid spots may contracts or expand during their spatio-temporal evolution. Stratification can be also measured by the *scale height*, i.e. a typical length scale, L_h , built in terms of mean hydrostatic quantities. In our case, the most natural way to define it is by using the temperature profile: $L_h = (T_u/\Delta T)L_z = L_z/Z$. Where we used the dimensionless parameter, $Z = \Delta T/T_u$ which is a direct measurement of the stratification effects: for $Z \gg 1$, the cell height L_z is much larger than the typical stratification length, i.e. the fluid is highly stratified. On the other hand, the limit $Z \rightarrow 0$ corresponds to the so-called Oberbeck-Boussinesq approximation, where both stratification and compressibility are vanishingly small. The latter is, by far, the most studied convection configuration, even though some important applications for astrophysics [45, 46] and recently also for laboratory set-up [47–49] cannot neglect compressible modes. It is possible to show [35] that in the Boussinesq approximation, the dependency from the polytropic index disappear (as it must obviously do) while it remains a possible effect induced by the adiabatic gradient (usually small on laboratory experiments, but not necessarily on atmospheric scales).

We use this complex set-up to benchmark the thermal-LBM algorithm proposed, and probe its robustness at changing compressibility. This can be done directly against exact results on the emergence of convective instability in the system. It is possible to calculate, in a closed form, the stability problem of the linearized system around the hydrostatic solution (14), for both slip or no-slip velocity boundary conditions and for any polytropic index [34]: these are just suitable extensions of the well known Rayleigh calculation made for the incompressible case [50]. Stratification makes the problem non-homogeneous (in the vertical direction) and therefore it is not possible to define in a unique way the Rayleigh number. Anyhow, it turns out that it is possible to introduce a height-dependent Rayleigh number which rules the linearized problem:

$$Ra(z) = \frac{(g/T_0(z))L_z^4(\beta - \beta_{ad})}{(k/\rho_0(z)c_p)(\nu/\rho_0(z))}, \quad (15)$$

and one can express the whole bifurcation diagram in terms the value of the Rayleigh number at a given height, say the middle of the cell $z = L_z/2$ for example: $\tilde{Ra} = Ra(L_z/2)$. Different works have been devoted to the calculations of the critical \tilde{Ra}_c at changing the polytropic index, the scale height, Z and the boundary conditions at the top/bottom plates [34, 51, 52]. A result of the stability calculation predicts that there exists a critical Rayleigh number which depends only on the polytropic index, m , on the stratification parameter, Z , and on the wavelength, a , of the perturbation, $\tilde{Ra}_c(m, Z, a)$. The hydrostatic solution will therefore become unstable under perturbation of a wavelength corresponding to the minimum possible critical Rayleigh number. Compressibility and stratification may have different effects, either stabilizing or destabilizing the systems, depending on the hydrostatic underlying equilibrium. For example, if the hydrostatic profile has an unstable density profile, $m < 0$, one gets that the critical Rayleigh decreases at increasing temperature jumps. The opposite happens when density is stably stratified, $m > 0$. From the definition of Rayleigh given in (15), it is easy to realize the importance of the adiabatic gradient, $\beta_{ad} = g/c_p$, i.e. if $\beta < \beta_{ad}$, the control parameter is always negative and the system will always be linearly stable. In figure 2 we show the result of a numerical search of the critical Rayleigh number (i.e. the onset of the transition to convection) using our LBM algorithm, obtained by exploring the long time behavior of the system, prepared with a small perturbation to its hydrostatic equilibrium, and monitoring the successive temporal growth/decline of the total kinetic energy (example in the inset). The LBM has been applied by imposing no-slip impenetrable boundary conditions for the velocity field at top/bottom walls, $u_z(z = \pm L_z/2) = 0$; $u_x(z = \pm L_z/2) = 0$; and with an imposed constant temperature jump, $T(z = -L_z/2) = T_d$; $T(z = L_z/2) = T_u$. Lateral boundaries are fully periodic. Technical

details on the way to implement the given boundary conditions in the LBM algorithm are given in Appendix B. In the same figure we also report the critical Rayleigh numbers obtained from the LBM exploration, compared with the exact analytical results obtained by solving numerically the eigenvalue problem for the linearized equations as given in [34]. As one can see, the agreement is good, even for large temperature jumps, up to $Z \sim 2$. Larger values of Z are difficult to reach, because of limitations imposed by numerical stability of the boundary conditions and by the growth of unstable compressible modes in the system. In order to overcome such limitation one should probably extend the Hermite projections to higher and higher orders [32]. The main error source in the determination of the critical Rayleigh number out of our LBM method stems from the presence of spurious, small, departure from the exact linear profile in the mean temperature close to the boundary walls. This departure goes together with the existence of small spurious transverse velocity for two-three grid layers close to the wall and are due to the existence of discrete velocities which connects up to three layers in the lattice inducing non-local boundary conditions effects (see appendix A and B for details). Such effects can be annoying for the investigation of highly turbulent regimes, where the boundary layer dynamics becomes crucial to drive the correct thermal exchange with the bulk [53]. This shortcoming can be strongly reduced by moving from LBM algorithms using exact streaming (as done here) to LBM based on finite-volume schemes [54]. Details in this direction will be published elsewhere. The small spurious oscillations close to the boundaries does not prevent to get a very good quantitative validation of the algorithms also when large scale convective rolls are present. For example in figure 3 we make a one-to-one comparison of the LBM numerics with a numerical study using finite-difference scheme for incompressible Rayleigh-Bénard systems [55, 56]. Again, the stationary profiles are perfectly superposing, as shown for both temperature and velocity in figure 3. This ends our validation section. In the next section we apply the new algorithm to study compressible dynamics, as it is the case of Rayleigh-Taylor instabilities in thermal stratified flows. In the latter case, the small spurious oscillations close to the walls are obviously completely unimportant, being the bulk the only physically interesting region.

IV. RAYLEIGH-TAYLOR SYSTEMS

Superposition of a heavy fluid above a lighter one in a constant acceleration field depicts a hydro-dynamic unstable configuration called the Rayleigh-Taylor (RT) instability [50] with applications on different fields going from inertial-confinement fusion [57] to supernovae explosions [58] and many others [59]. Although this instability was studied for decades it is still an open problem in several aspects [60]. In particular, it is crucial to control the initial and late evolution of the mixing layer between the two miscible fluids; the small-scale turbulent fluctuations, their anisotropic/isotropic ratio; their dependency on the initial perturbation spectrum or on the physical dimensions of the embedding space [61, 62]. In many cases, especially concerning astrophysical and nuclear applications, the two fluids evolve with strong compressible and/or stratification effects, a situation which is difficult to investigate either theoretically or numerically. Here, we concentrate on the large scale properties of the mixing layer, studying a slightly different RT system than what usually found in the literature: the spatio temporal evolution of a single component fluid when initially prepared on the hydrostatic unstable equilibrium, i.e. with a cold uniform region in the top half and a hot uniform region on the bottom half (see bottom panel of figure 1). For the sake of simplicity we limit the investigation to the 2d case. While small-scales fluctuations may be strongly different in 2d or 3d geometries, the large scale mixing layer growth is not supposed to change its qualitative evolution [63, 64]. A grey-scale coded snapshot of a typical RT run is shown in figure 4 showing all the complexity of the phenomena. Let us start to define precisely the initial set-up. We prepare a single component compressible flow in a 2d tank of size, $L_x \times L_z$, with adiabatic and no-slip boundary conditions on the top and bottom walls, and with periodic boundary conditions on the vertical boundaries. For convenience we define the initial interface to be at height $z = 0$, the box extending up to $z = L_z/2$ above and $z = -L_z/2$ below it (see figure 1). In the two half volumes we then fix two different homogeneous temperature, with the corresponding hydrostatic density profiles, ρ_0 , verifying [65]:

$$\partial_z p_0(z) = -g\rho_0(z). \quad (16)$$

Considering that in each half we have $p_0(z) = T\rho_0(z)$, with T fixed, the solution has an exponentially decaying behavior in the two half volumes, each one driven by its own temperature value. The initial hydrostatic unstable configuration is therefore given by:

$$\begin{cases} T_0(z) = T_u; \rho_0(z) = \rho_u \exp(-g(z - z_c)/T_u); & z > 0 \\ T_0(z) = T_d; \rho_0(z) = \rho_b \exp(-g(z - z_c)/T_d); & z < 0. \end{cases} \quad (17)$$

To be at equilibrium, we require to have the same pressure at the interface, $z = z_c = 0$; which translates in a simple condition on the prefactor of the above expressions:

$$\rho_u T_u = \rho_b T_d. \quad (18)$$

Because $T_u < T_d$, we have at the interface $\rho_u > \rho_b$. As far as we know, there are no exhaustive detailed calculations of the stability problem for such configuration, even though not too different from the usual RT compressible case [50, 66, 67]. As said, this is not the common way to study RT systems, which is usually meant as the superposition of two different miscible fluids, isothermal, with different densities [50, 61, 66, 68]. As far as compressible effects are small, one may safely neglect pressure fluctuations and write – for the case of an ideal gas:

$$\frac{\delta\rho}{\rho} \sim -\frac{\delta T}{T} \quad (19)$$

and the two RT experiments are then strictly equivalent. Moreover, in the latter case, if one may neglect the dependency of viscosity and thermal diffusivity from temperature, the final evolution is indistinguishably from the evolution of the temperature in the Boussinesq approximation [62, 63]. Here we will study both the case of small compressibility and small stratification, where pressure is always close to its hydrostatic value, $p \sim p_0$, and the case when compressibility becomes dynamically relevant, changing the global large scale evolution of the mixing layer.

A. RT instability in thermally active flows: the role of the adiabatic gradient

The main novelty in the set up here investigated is due to the presence of new effects induced by the adiabatic gradient, which in our case can be written as in the previous Section $\beta_{ad} = g/c_p$. In order to understand the main physical point it is useful to think at the RT mixing layer as equivalent to a (developing) Rayleigh-Bénard system with an imposed mean temperature gradient [69, 70]. Let us denote with $L_{ml}(t)$ the typical width of the RT mixing layer at a given time as measured for example from the distance between the two elevations where the mean temperature profile is 1% lower or higher than the bottom and top, respectively, unmixed temperature values, $L_{ml} = z_u - z_d$, where $\langle T(x, z_u) \rangle_x = 1.01T_u$ and $\langle T(x, z_d) \rangle_x = 0.99T_d$. It is well known that the temperature tends to develop a linear profile inside the mixing region, the resulting instantaneous temperature gradient is then given by $\beta(t) = (T_d - T_u)/L_{ml}(t)$, and it decreases in time inversely to the growth of the mixing length. As a result, soon or later (if the box is tall enough) the instantaneous temperature gradient will become of the same order of the adiabatic gradient, $\beta(t) \sim \beta_{ad}$ and the growth of the mixing length will stop. One can define an instantaneous Rayleigh number, driving the physics inside the mixing layer, estimated as in Section III:

$$\tilde{Ra}(t) = \frac{(g/\tilde{T}_0)L_{ml}^4(t)(\beta(t) - \beta_{ad})}{(k/\tilde{\rho}_0 c_p)(\nu/\tilde{\rho}_0)}, \quad (20)$$

where $\tilde{(\cdot)}$ indicates quantities evaluated at the middle layer. It is clear that for small times, $\beta(t) \ll \beta_{ad}$, the effective instantaneous Rayleigh number is high: the system is unstable, and the mixing length grows. On the other hand, as time elapses, the vertical mean temperature gradient decreases, until a point when, $\beta(t) \sim \beta_{ad}$, the instantaneous effective Rayleigh number becomes $\tilde{Ra}(t) \sim \mathcal{O}(1)$ and the system tends to be stabilized. We can then identify an *adiabatic length*:

$$L_{ad} = (T_d - T_u)/\beta_{ad} = c_p \Delta T / g$$

which determines the maximum length achievable by the mixing layer, in our configuration. Let us notice that in absence of the adiabatic gradient, the Rayleigh number would continue to grow indefinitely, being proportional to the third power of $L_{ml}(t)$, as it is the case for usual RT systems. If the profile coinciding with the adiabatic gradient is going to be fully stable depends on the top/bottom boundary conditions imposed on the whole spatial domain. In any case, when temperature matches the adiabatic profile, the system strongly feel it, showing a sudden slowing down of the mixing layer growth. To our knowledge, this effect has never been predicted before, within this framework. We show in figure 5 the evolution of temperature profiles when adiabatic effects are important. It is clear how the mixing layer growth is strongly slowed down when $L_{ml}(t) \sim L_{ad}$; afterward only very slow relaxation process happens further, mainly at the border between the edge of the mixing layer and the fluids region with homogeneous temperature. A possible way to estimate quantitatively when and how the adiabatic gradient starts to play a role in the growth of the mixing length is to use a simple phenomenological closure for large scale quantities in the system. We start from the self-similar scaling predicted by [71, 72] for the homogeneous not stratified growth:

$$(\dot{L}_{ml}(t))^2 = 4\alpha^{(L)} g A t L_{ml}(t) \quad (21)$$

which has a unique solution (beside the trivial one, $L_{ml} = 0$) in terms of the initial value, $L_{ml}(t_0)$:

$$L_{ml}(t) = L_{ml}(t_0) + 2\sqrt{L_{ml}(t_0)\alpha^{(L)} A t g (t - t_0) + \alpha^{(L)} A t g (t - t_0)^2}. \quad (22)$$

Eq. (21) offers the advantage to be local in time, i.e. one may extract the value of $\alpha^{(L)}$ by a simple evaluation of the plateau in the ratio $(\dot{L}_{ml})^2/L_{ml}$, time by time. In order to minimally modify the above expression considering the saturation effects induced by stratification, we propose to use:

$$(\dot{L}_{ml}(t))^2 = 4\alpha^{(L)} g At L_{ml}(t) \psi \left(\frac{L_{ml}(t)}{L_{ad}} \right) \quad (23)$$

where $\psi = \psi(x)$ must be a function fulfilling the condition $\psi \rightarrow 1$ as $x \rightarrow 0$ (that is for $L_{ad} \rightarrow \infty$), in order to recover the equation (21) for the not stratified case when the adiabatic gradient goes to zero. We further add the requirement of reaching the adiabatic profile with zero velocity and acceleration, enforcing a strict irreversible growth, i.e. $\dot{L}_{ml} \geq 0$, as it must be for the case of miscible fluids. Under these assumptions, it can be shown that the simplest form for the function ψ is:

$$\psi \left(\frac{L}{L_{ad}} \right) = C \left[e^{-\left(\frac{L-L_{ad}}{L_{ad}} \right)} - \left(\frac{2L_{ad}-L}{L_{ad}} \right) \right] \quad (24)$$

where the prefactor C must be set equal to $1/(e-2)$ to comply with the prescribed boundary conditions. Equation (23) must be considered as a zero-th order phenomenological way to take into account of the adiabatic gradient in the mixing layer evolution.

We integrated numerically eq. (23) testing the result in figure 6 where we show that it is possible to fit the global evolution of the mixing length $L_{ml}(t)$, by using reasonable [60] values of $\alpha^{(L)}$, for all times, including the long time behavior where $L_{ml}(t) \sim L_{ad}$. In the same figure, we also show the behaviour of the time-dependent effective Rayleigh number (20), estimated using the instantaneous mixing length, $L_{ml}(t)$. As one can see, after the initial monotonic growth of the turbulent intensity, there appear a sudden slowing down, as identified by a strong reduction in the effective Rayleigh number. We can therefore safely assume that the solution of our equation (23) is a good generalization of (22) including also the adiabatic gradients effects.

B. Compressible effects and mixing layer growth

As shown in the previous section, effects induced by the adiabatic gradient start to appear when the mixing length becomes of the order of the adiabatic length $L_{ml}(t) \sim L_{ad}$. It is nevertheless possible to study the limit $L(t) \ll L_{ad}$ but still observing important effects due to compressibility. Indeed, compressibility due to stratification is controlled by the Atwood number. From the expression of the instantaneous Rayleigh number (20) one may compute the typical length scale at which turbulence will be maximal, i.e. the largest extension of the mixing layer up to which the Rayleigh number is still growing, before decreasing because of the adiabatic gradient. This is just given by the maximum of $\tilde{Ra}(t)$ as a function of time, which is reached at a characteristic time, t^* such that:

$$L_{ml}(t^*) = \frac{3}{4} L_{ad} = \frac{3 c_p \Delta T}{4 g}. \quad (25)$$

It is also possible to estimate the typical Mach number reached at the maximal turbulent intensity, considering that hydrodynamical velocities can be estimated as, $V_{max} \sim d/dt L_{ml}(t^*) = 2\alpha^{(L)} At g t^*$ and that the minimal sound speed is given, in our units, by $v_s = \sqrt{T_d}$, we get for the Mach number at the maximal turbulent intensity: $Ma \sim At \sqrt{\alpha^{(L)} c_p}$ where we have used (22) to estimate t^* at a given $L_{ml}(t^*)$. As a result, dynamical compressibility is only driven by the Atwood number -at fixed c_p . Using the typical values of $\alpha^{(L)} \sim 5 \cdot 10^{-2}$, as reported in the literature [60], and plugging the correct prefactor, we estimate $Ma \sim 0.4$, for the largest Atwood we could achieve, $At \sim 0.4$. It is well known that compressibility effects break the up/down symmetry in the mixing layer propagation [71, 72], downwards spikes (cold fluid blobs) move faster than upwards bubbles (hot fluid blobs). Such effect is completely missing in Boussinesq approximation where there is a perfect up/down symmetry, by definition.

Neglecting slowing down effects induced by the adiabatic gradients, i.e. limiting the study of the mixing layer growth up to $L_{ml}(t) \ll L_{ad}$, we may investigate the symmetry breaking in our set up at changing the Atwood number. To give an idea of the effects of compressibility, we show in figure 7 a few instantaneous mean profile of temperature, density and pressure for the two Atwood numbers here investigated. From the density and temperature profiles it is easy detectable, already by naked eyes, the asymmetry present for the high Atwood case $At = 0.4$ in the growth of the mixing layer, with the colder and denser front moving faster. Also, the appearance of non-trivial fluctuations in the pressure around the hydrostatic profile, for the case at $At = 0.4$, are the clear evidence of compressible effects at play. Both the asymmetry and the pressure fluctuations are completely absent for the case at small Atwood (left panels of figure 7, an evidence of Boussinesq-like thermal fluctuations). All numerical experiments have been performed by

preparing the initial configuration in its hydrostatic equilibrium (17) plus a smooth interpolation between the two half volumes in order to have a finite width of the initial interface. The initial temperature profile is therefore chosen to be:

$$T_0(z) = \frac{T_u + T_d}{2} + \frac{T_u - T_d}{2} \tanh\left(\frac{(z - z_c)}{w}\right)$$

where with w we define the initial width of the interface and z_c its unperturbed height ($z_c = 0$ in our frame of reference). Initial density $\rho_0(z)$ and pressure $p_0(z)$ are then fixed by solving the hydrostatic equation (16) in order to get the hydrostatic solution corresponding to the smoothed temperature profile.

To destabilize the initial configuration, we follow [73] and shift randomly the center of the interface by adding horizontal perturbation at different wavelengths in the range $k \in [k_{min} : k_{max}]$:

$$z_c \rightarrow z_c(x) = \frac{\epsilon}{N} \sum_{k=k_{min}}^{k=k_{max}} \cos(2\pi k x / L_x + \phi_k) \quad (26)$$

where ϕ_k are random phases and $N = \sqrt{k_{max} - k_{min}}$, in order to have a total amplitude for the initial width almost independent on the number of modes. We have tried different ranges of wavelengths, without observing quantitative differences in the large time growth of the mixing layer. The ratio $W = \epsilon/w$ gives the “wiggling” of the interface, i.e. how much the perturbation of the interface position is important with respect to the interface width.

Below, we present results in different geometry, up to a resolution of $L_x \times L_z = 1664 \times 4400$ with different choices of W . For each parameters set we made typically $\mathcal{O}(50)$ separate RT evolution, starting from different random phases initial configurations.

In the sequel, we show a summary of the results from two typical numerical series of runs, one with $At = 0.05$ (small compressibility) and a second one with $At = 0.4$ (large compressibility). It is useful to adopt a different definition for the mixing length in terms of a bulk mixing percentage, introducing the characteristic function (tent-map):

$$\begin{cases} \chi[\xi] = 2\xi; & 0 \leq \xi \leq 1/2 \\ \chi[\xi] = 2(1 - \xi); & 1/2 \leq \xi \leq 1 \end{cases} \quad (27)$$

and defining the mixing length as [72]:

$$H(t) = \frac{1}{L_x} \int dx dz \chi \left[\frac{T(x, z) - T_u}{T_d - T_u} \right]. \quad (28)$$

It is easy to realize that if the temperature is fully homogenized in the fluid, $T(x, z) = (T_u + T_d)/2$, then the mixing length coincides with the full vertical extension of the box: $H = L_z$; if we have two perfectly separated hot and cold regions we have $H = 0$. In the intermediate situation when we have a mean linear temperature profile for $z \in [z_d, z_u]$, between two unmixed regions ($T = T_u$ if $z > z_u$ and $T = T_d$ if $z < z_d$) the mixing length estimated by (27) is exactly given by half of the linear region, $H = (z_u - z_d)/2$. The definition of the mixing length (27) must be preferred with respect to more common definition of L_{ml} based on thresholds on the linear profile, as adopted in the previous section. The former, being based on a bulk measure is not affected too much on the highly fluctuating properties of the interface between mixed and unmixed fluids. This is particularly important in 2d, where the averaged profile, being a one-dimensional cut, may fluctuate a lot (see also figure 7). Anyhow, in the case of a perfectly linear temperature profile the two lengths are obviously related by the relation $H = 1/2\delta L_{ml}$, where δ is the percentage threshold used to identify the mixing front (in the previous section $\delta = 0.99$).

Moreover, because here we want to distinguish the downward growth of the front due to cold spikes from the upward growth of bubbles, we introduce two different integral mixing lengths:

$$\begin{aligned} H_s(t) &= \frac{1}{L_x} \int dx dz \left(\Theta \left(\frac{L}{2} - z \right) \chi \left[\frac{T(x, z) - T_u}{T_d - T_u} \right] \right); \\ H_b(t) &= \frac{1}{L_x} \int dx dz \left(\Theta \left(z - \frac{L}{2} \right) \chi \left[\frac{T(x, z) - T_u}{T_d - T_u} \right] \right); \end{aligned}$$

where of course, $H(t) = H_s(t) + H_b(t)$. Clearly, the $\alpha^{(H)}$ value ruling the long term quadratic growth of the integral mixing H is not necessarily the same of L_{ml} . Typically one expects the same relation $\alpha^{(H)} = 0.5\delta\alpha^{(L)}$ valid for the definition of the two mixing length, at least for times long enough.

As one can see in figure 8 there is a wide scattering of the mixing length evolution from run to run, where the only differences between them is the realization of the initial random phases. Due to the intense local temperature and density fluctuations, averaging over horizontal direction is not very efficient to smooth down statistical fluctuations, and one observes high variations from sample to sample: many realizations are needed to extract stable quantitative results on the long time evolution. In order to have an insight on the typical fluctuations we decided to analyze run by run and following two fitting procedures. First, we start from the equivalent of (22), written for bubbles and spikes separately:

$$\begin{cases} H_b(t - t_0) = H_b(0) + \dot{H}_b(0) t + \alpha_b^{(H)} At g t^2 \\ H_s(t - t_0) = H_s(0) + \dot{H}_s(0) t + \alpha_s^{(H)} At g t^2 \end{cases} \quad (29)$$

with $\dot{H}_{b,s}(0) = 2 \sqrt{H_{b,s}(0) \alpha_{b,s}^{(H)} At g}$, where t_0 must be understood as the time when the initial perturbation is fully entered in its non-linear regime. In other words, t_0 must be larger than the typical characteristic time of the slowest unstable mode. It can be estimated from linear stability analysis as $t_0 \sim \sqrt{L_x / (2\pi g At)}$. A brute force way to extract the growth rate is to evaluate the ratio $\alpha_{s,b}^{(H)} = \lim_{t \rightarrow \infty} H_{s,b}(t) / t^2$. Even, neglecting possible contamination due to stratification, this is of course valid, only asymptotically, when both dependencies on the initial time t_0 and on the initial mixing length $H_{s,b}(t_0)$ become negligible. As a matter of fact, taking into account also the maximum time achievable due to numerical limitations, it is very difficult to extract stable statistical results on the $\alpha^{(H)}$ fluctuations starting from the brute force analysis of (29). For instance, we found that a parabolic fit to our data, taking $\alpha_{s,b}^{(H)}$ free is very sensitive to the initial time t_0 and/or the initial distance $H_{b,s}(t_0)$, without allowing for a systematic assessment of the asymptotic behaviour. To give an idea of the importance of the initial condition versus statistical fluctuations, we show in the bottom panel of figure 9 the results of the asymptotic ratio $H_{s,b}(t) / t^2$ for two different series of runs with different initial conditions. As one can see, even if asymptotically there is a clear tendency to forget the initial separation, in agreement with (29) there is not a well developed plateau, up to the time achievable in our numerics, indicating the existence of important sub-leading effects. The existence of such terms is highlighted in the inset of the same panel, where a log-log plot clearly shows the lack of a plateau even for large times.

Another alternative, and more robust way, to extract $\alpha^{(H)}$ relies on the differential equivalent of (29) given by (21) or (23) when stratification becomes important. Using (21), one may directly assess the non-linear growth rate, without spurious contamination from initial conditions.

In the upper panel of figure 9 we show the same data plotted in the lower panel but for the ratio

$$\alpha_{s,b}^{(H)} = (\dot{H}_{s,b}(t))^2 / (4g At H_{s,b}(t)), \quad (30)$$

i.e. we address time-by-time the part depending on asymptotic growth rate only. It is evident the net improvement in both the extension of the range where $\alpha^{(H)}$ coefficients are constant and the clear disentanglement of effects coming from the initial conditions. Out of the data for $(\dot{H}_{s,b}(t))^2 / 4 (g At H_{s,b}(t))$ we may estimate the statistical fluctuations of $\alpha_{s,b}^{(H)}$, by making a fit to a constant in a given time windows. In figure 10 we plot the results of fitting the evolution (30) independently for bubbles or spikes (upward or downward fronts). From this we learn a few interesting facts: (i) at small Atwood (upper panel) bubbles and spikes travels almost with the same statistics, even though a small asymmetry can be observed in the shape of the whole histogram. The asymmetry is so small, that if averaged quantities are measured, the differences between them falls within error bars; (ii) there are not important effects from initial conditions -compare the two upper panels obtained with two different classes of initial conditions-; at least when data are fitted using (30), confirming that the observed spatio-temporal evolutions is dominated by strongly non-linear fully developed dynamic; (iii) at large Atwood (lower panel) the asymmetry becomes evident, spikes are systematically faster than bubbles, the two evolutions gives different mean values for $\alpha_s^{(H)}$ and $\alpha_b^{(H)}$ parameter. Our measure of the average global growth rate $\alpha^{(H)}$, can be estimated by summing up the growth rate in the two half cells: $\alpha^{(H)} = \alpha_s^{(H)} + \alpha_b^{(H)} \sim 0.02$ is in agreement with values typically found in literature [60, 71, 72]. For instance, in [60] a detailed overview of numerical results gives for the growth rate of bubbles, measured on the 99% width, $\alpha_b^{(L)} \sim 0.025 \pm 0.003$, in agreement with $\alpha_b^{(H)} = 0.0095 \pm 0.002$ we found for our integral growth rate (see caption of figure 10) taking into account that by definition one expects a factor two between the measurement made on the integral quantity, $\alpha^{(H)}$, and the measurement made on the 99% level set, $\alpha^{(L)}$.

The last issue we want to discuss concerns with homogenization inside the mixing layer. It is easy to show that in the Boussinesq approximation for a convective stationary cell with a mean linear temperature profile, all deviations from the mean profiles are homogeneous. The case of RT evolutions investigated here is slightly different. First, whenever stratification is important, there is no reason to expect exactly homogenization inside the mixing length.

Second, and more importantly, homogeneity must be expected only well inside the mixing layer, far from the up and downside fronts, where clearly strong non-homogeneous effects for both mean and fluctuating quantities must appear. It is interesting therefore to test, how homogeneous the statistics is, also to quantify the degree of mixing. In order to do that, we introduce the p -th order moments of temperature fluctuations:

$$Q^{(p)}(z, t) = \langle (T(x, z) - \langle T(x, z) \rangle_x)^p \rangle_x. \quad (31)$$

In figure 11 we show the root mean square fluctuations around the vertical mean temperature profile, $Q^{(2)}(z, t)$, (bottom panel) and the flatness, $F(z, t) = Q^{(4)}(z, t)/(Q^{(2)}(z, t))^2$, i.e. the ratio between fourth and squared second order moments of fluctuating quantities (top panel). As one can see, the root mean square fluctuations tend –very slowly– to develop a flatter and flatter plateau inside the mixing region, demonstrating that if the mixing layer is wide enough, there will be a larger and larger region where statistics is pretty homogeneous. On the other hand, if we plot the Flatness as a function of a normalized mixing length width, it converges towards a self-similar profile, for any time, where the effects coming from the two boundaries of the mixing regions are felt inside the whole layer, without showing any trend towards homogenization. This second finding is a clear indication that if normalized with the total mixing length extension, the region where the statistics may be considered homogeneous does not increase with time.

V. CONCLUSIONS AND PERSPECTIVES

We have explicitly computed the continuum thermo-hydrodynamical limit of a new formulation of Lattice Kinetic equations for thermal compressible flows, recently proposed in [33]. We have shown that the hydrodynamical manifold is given by the correct compressible Fourier-Navier-Stokes equations for a perfect fluid. We have validated the calculations against exact results for transition to convection in Rayleigh-Bénard compressible systems and against direct comparison with finite-difference methods. The method is stable and quantitatively reliable up to temperature jumps between top and bottom walls (stratification) of the order of $\Delta T/T_u \sim 2$. We have also applied the method to study Rayleigh-Taylor instability for compressible stratified flows and we determined the growth of the *asymmetric* mixing layer at changing Atwood numbers up to $At \sim 0.4$ and to Rayleigh $Ra \sim 2 \times 10^{10}$. We determined the distribution of the growth rate for bubbles and spikes, at changing At and we discuss its dependence on the initial perturbation. We also discussed the importance of the adiabatic gradient for the growth of the RT mixing layer in strongly stratified systems. In the latter case, we showed the existence of a maximal width, the adiabatic length, L_{ad} , for the mixing region. The high flexibility –and locality– of LB algorithm makes them the ideal playground where to push the resolution, having perfectly scalable performances as a function of the number of processors in the parallel architecture. In particular, it is simple to extend such algorithm to deal with fully 3d systems for ideal, non-ideal and/or even immiscible two fluids systems. High resolution studies of Rayleigh-Taylor systems meant to investigate short wavelengths scaling properties of velocity, density and temperature fields for high Rayleigh, with and without surface tension [39], and using a highly optimized LBM algorithm for the Cell Broadband Engine [75] are under current investigation and will be reported elsewhere [76]. The thermal LBM here proposed still suffers of small spurious oscillations of temperature and perpendicular velocity close to the solid boundaries, making it still not appropriate to study high Rayleigh numbers stationary convection. A possible way to overcome this difficulty consists in abandoning numerical schemes based on exact streaming and to develop the proposed thermal LBM on a finite volume scheme. Results in this direction are out of the scope of this paper and will be the subject of a forthcoming publications.

Acknowledgments: We thank R. Benzi, G. Boffetta, A. Celani, H. Chen, S. Gauthier, A. Mazzino and X. Shan for useful discussions. We acknowledge partial computational support from “Centro Enrico Fermi”, from CASPUR (Roma, Italy, HPC grant n. std09-327), from CINECA (Bologna, Italy) and SARA (Amsterdam, The Netherlands). This work was carried out under the HPC-EUROPA2 project (project number: 228398) with the support of the European Commission Capacities Area - Research Infrastructures Initiative. AS thanks FT and the Technical University of Eindhoven for hospitality during his HPC-EUROPA visit.

VI. APPENDIX A

In this appendix we detail the steps of the Chapman Enskog expansion leading to the thermohydrodynamical equations under the effect of general forcing term $\rho \mathbf{g}$. Similar analysis (without the effect of the forcing) can be found in [40]. We start from the shifted equilibrium formulation

$$f_l(\mathbf{x} + \mathbf{c}_l \Delta t, t + \Delta t) - f_l(\mathbf{x}, t) = -\frac{\Delta t}{\tau} (f_l(\mathbf{x}, t) - \bar{f}_l) \quad (32)$$

where, for the sake of simplicity, in the notation of this appendix we have renamed the equilibrium distribution function with shifted fields, $f_l^{(eq)} = \bar{f}_l$:

$$\bar{f}_l = \bar{f}_l(\rho, \mathbf{u}^{(L)} + \boldsymbol{\chi}, T^{(L)} + \lambda)$$

and where $\boldsymbol{\chi}$ and λ are general momentum and temperature shifts for the equilibrium distribution with $\mathbf{u}^{(L)}, T^{(L)}$ the lattice velocity and temperature hereafter denoted simply with \mathbf{u} and T . Central to our analysis is the expansion of the equilibrium distribution in Hermite polynomials [15, 26, 40]

$$\bar{f}_l = w_l \sum_n \frac{1}{n!} \mathbf{a}_0^{(n)}(\rho, \mathbf{u} + \epsilon \boldsymbol{\chi}, T + \epsilon^2 \lambda) \mathcal{H}_l^{(n)}$$

with w_l suitable weights whose values are reported in [26, 29] for the $D2Q37$ model here used (see also figure 12). For the purposes of our investigation a fourth order approximation proves to be enough to recover the correct equations with the right isotropic properties for all hydrodynamical fields and tensors up to the eighth order [29]. The Hermite polynomials are given by the following relations:

$$\mathcal{H}_l^{(0)} = 1; \quad \mathcal{H}_l^{(1)} = \mathbf{c}_l; \quad \mathcal{H}_l^{(2)} = \mathbf{c}_l^2 - \delta \quad (33)$$

$$\mathcal{H}_l^{(3)} = \mathbf{c}_l^3 - \delta \mathbf{c}_l; \quad \mathcal{H}_l^{(4)} = \mathbf{c}_l^4 - \delta \mathbf{c}_l^2 + \delta \delta \quad (34)$$

and the projection coefficients $\mathbf{a}_0^{(n)}$ by

$$\left\{ \begin{array}{l} \mathbf{a}_0^{(0)} = \rho \\ \mathbf{a}_0^{(1)} = \rho \mathbf{u} + \epsilon \rho \boldsymbol{\chi} \\ \mathbf{a}_0^{(2)} = \rho[\mathbf{u}^2 + (T-1)\delta] + \epsilon \rho \boldsymbol{\chi} \mathbf{u} + \epsilon^2(\rho \boldsymbol{\chi}^2 + \rho \delta \lambda) \\ \mathbf{a}_0^{(3)} = \rho[\mathbf{u}^3 + (T-1)\delta \mathbf{u}] + \epsilon(\rho \boldsymbol{\chi} \mathbf{u}^2 + \rho(T-1)\delta \boldsymbol{\chi}) + \epsilon^2(\rho \boldsymbol{\chi}^2 \mathbf{u} + \rho \lambda \delta \mathbf{u}) + \epsilon^3(\rho \boldsymbol{\chi}^3 + \rho \lambda \delta \boldsymbol{\chi}) \\ \mathbf{a}_0^{(4)} = \rho[\mathbf{u}^4 + (T-1)\delta \mathbf{u}^2 + (T-1)^2 \delta^2] + \epsilon(\rho \boldsymbol{\chi} \mathbf{u}^3 + \rho(T-1)\delta \boldsymbol{\chi} \mathbf{u}) + \epsilon^2(\rho \boldsymbol{\chi}^2 \mathbf{u}^2 + \rho \lambda \delta \mathbf{u}^2 + \rho(T-1)\delta \boldsymbol{\chi}^2) + \epsilon^3(\rho \boldsymbol{\chi}^3 \mathbf{u} + \rho \lambda \delta \boldsymbol{\chi} \mathbf{u}) + \epsilon^4(\rho \boldsymbol{\chi}^4 + \rho \lambda \delta \boldsymbol{\chi}^2) \end{array} \right.$$

where the shorthand notations of Grad [15, 74] for fully symmetric tensors are adopted. A possible set of *on-site* space-filling lattice velocities can be found in figure 12 and fully detailed in [15, 26, 30]. If one gives up the requests to have lattice velocities only on grid points and allows also for out of lattice discretized velocity sets, the number of vectors needed to recover isotropy for moments up to order eight can be reduced [30]. We next introduce [37] a small separation of scale parameter ϵ and consider the expansion in ϵ for the distribution function

$$f_l = f_l^{(0)} + \epsilon f_l^{(1)} + \epsilon^2 f_l^{(2)} + \epsilon^3 f_l^{(3)} + \epsilon^4 f_l^{(4)} + \dots \quad (35)$$

and the rescaling of the time-space derivatives

$$\partial_t \rightarrow \epsilon \partial_{1t} + \epsilon^2 \partial_{2t} + \mathcal{O}(\epsilon^3); \quad \partial_i \rightarrow \epsilon \partial_i. \quad (36)$$

This allows to rewrite the streaming term in the lattice Boltzmann equation as

$$f_l(\mathbf{x} + \mathbf{c}_l \Delta t, t + \Delta t) - f_l(\mathbf{x}, t) = \epsilon A_1 + \epsilon^2 A_2 + \epsilon^3 A_3 + \dots$$

where for our purposes it is enough to consider terms up to A_2

$$\left\{ \begin{array}{l} A_1 = (\partial_{1t} f_l^{(0)} + c_l^i \partial_{1t} \partial_i f_l^{(0)}) \Delta t \\ A_2 = (\partial_{2t} f_l^{(0)} + \partial_{1t} f_l^{(1)} + c_l^i \partial_i f_l^{(1)}) \Delta t + \frac{1}{2} (c_l^i c_l^j \partial_i \partial_j f_l^{(0)} + c_l^i \partial_i \partial_{1t} f_l^{(0)} + c_l^i \partial_i \partial_{1t} f_l^{(0)} + \partial_{1t} \partial_{1t} f_l^{(0)}) \Delta t^2. \end{array} \right.$$

If we further rescale the shifting [37] fields as

$$\mathbf{u} \rightarrow \mathbf{u} + \epsilon \boldsymbol{\chi}; \quad T \rightarrow T + \epsilon^2 \lambda \quad (37)$$

the shifted equilibrium can be further seen as a power series in ϵ

$$\bar{f}_l(\rho, \mathbf{u} + \epsilon \boldsymbol{\chi}, T + \epsilon^2 \lambda) = \bar{f}_l^{(0)} + \epsilon \bar{f}_l^{(1)} + \epsilon^2 \bar{f}_l^{(2)} + \epsilon^3 \bar{f}_l^{(3)} + \epsilon^4 \bar{f}_l^{(4)} + \dots$$

with

$$\left\{ \begin{aligned} \frac{\bar{f}_l^{(0)}}{w_l} &= \rho \mathcal{H}_l^{(0)} + \rho \mathbf{u} \mathcal{H}_l^{(1)} + \frac{1}{2} \rho [\mathbf{u}^2 + (T-1) \boldsymbol{\delta}] \mathcal{H}_l^{(2)} \\ &\quad + \frac{1}{6} \rho [\mathbf{u}^3 + (T-1) \boldsymbol{\delta} \mathbf{u}] \mathcal{H}_l^{(3)} \\ &\quad + \frac{1}{24} \rho [\mathbf{u}^4 + (T-1) \boldsymbol{\delta} \mathbf{u}^2 + (T-1)^2 \boldsymbol{\delta}^2] \mathcal{H}_l^{(4)} \\ \frac{\bar{f}_l^{(1)}}{w_l} &= \rho \boldsymbol{\chi} \mathcal{H}_l^{(1)} + \frac{1}{2} \rho \boldsymbol{\chi} \mathbf{u} \mathcal{H}_l^{(2)} \\ &\quad + \frac{1}{6} (\rho \boldsymbol{\chi} \mathbf{u}^2 + \rho (T-1) \boldsymbol{\delta} \boldsymbol{\chi}) \mathcal{H}_l^{(3)} \\ &\quad + \frac{1}{24} (\rho \boldsymbol{\chi} \mathbf{u}^3 + \rho (T-1) \boldsymbol{\delta} \boldsymbol{\chi} \mathbf{u}) \mathcal{H}_l^{(4)} \\ \frac{\bar{f}_l^{(2)}}{w_l} &= \frac{1}{2} (\rho \boldsymbol{\chi}^2 + \rho \boldsymbol{\delta} \lambda) \mathcal{H}_l^{(2)} + \frac{1}{6} (\rho \boldsymbol{\chi}^2 \mathbf{u} + \rho \lambda \boldsymbol{\delta} \mathbf{u}) \mathcal{H}_l^{(3)} \\ &\quad + \frac{1}{24} (\rho \boldsymbol{\chi}^2 \mathbf{u}^2 + \rho \lambda \boldsymbol{\delta} \mathbf{u}^2 + \rho (T-1) \boldsymbol{\delta} \boldsymbol{\chi}^2) \mathcal{H}_l^{(4)} \\ \frac{\bar{f}_l^{(3)}}{w_l} &= \frac{1}{6} (\rho \boldsymbol{\chi}^3 + \rho \lambda \boldsymbol{\delta} \boldsymbol{\chi}) \mathcal{H}_l^{(3)} + \frac{1}{24} (\rho \boldsymbol{\chi}^3 \mathbf{u} + \rho \lambda \boldsymbol{\delta} \boldsymbol{\chi} \mathbf{u}) \mathcal{H}_l^{(4)} \\ \frac{\bar{f}_l^{(4)}}{w_l} &= \frac{1}{24} (\rho \boldsymbol{\chi}^4 + \rho \lambda \boldsymbol{\delta} \boldsymbol{\chi}^2) \mathcal{H}_l^{(4)} \end{aligned} \right.$$

where, upon dimensional considerations, we have requested that when the forcing rescales as ϵ , the temperature shifting term is rescaling like ϵ^2 (see also [37] for a more detailed discussion). Using the Taylor expansion of $f_l(\mathbf{x} + \mathbf{c}_l \Delta t, t + \Delta t)$, we can impose the consistency in (32) order by order in ϵ :

$$\left\{ \begin{aligned} \mathcal{O}(\epsilon^0) : f_l^{(0)} &= \bar{f}_l^{(0)} \\ \mathcal{O}(\epsilon^1) : \partial_{1t} f_l^{(0)} + c_l^i \partial_i f_l^{(0)} &= -\frac{1}{\tau} (f_l^{(1)} - \bar{f}_l^{(1)}) \\ \mathcal{O}(\epsilon^2) : \partial_{2t} f_l^{(0)} + \partial_{1t} f_l^{(1)} + c_l^i \partial_i f_l^{(1)} + (\frac{1}{2} c_l^i c_l^j \partial_i \partial_j f_l^{(0)} \\ &\quad + \frac{1}{2} c_l^i \partial_i \partial_{1t} f_l^{(0)} + \frac{1}{2} c_l^i \partial_i \partial_{1t} f_l^{(0)} + \frac{1}{2} \partial_{1t} \partial_{1t} f_l^{(0)}) \Delta t \\ &= -\frac{1}{\tau} (f_l^{(2)} - \bar{f}_l^{(2)}). \end{aligned} \right. \quad (38)$$

Taking the momenta at the zeroth order in ϵ we can find some constraints for the higher terms in the expansion in of the distribution function. Since we know that $f_l^{(0)} = \bar{f}_l^{(0)}$, it follows from the definition of macroscopic fields that

$$\sum_l f_l^{(n)} = 0 \quad \sum_l c_l^i f_l^{(n)} = 0 \quad \sum_l c_l^2 f_l^{(n)} = 0 \quad n \geq 1.$$

1. Zeroth order

At the zeroth order in ϵ we can find some constraints for the higher terms in the expansion of the distribution function. We know that

$$f_l^{(0)} = \bar{f}_l^{(0)}.$$

It follows that, since we define our macroscopic variables as

$$\rho = \sum_l f_l; \quad \rho u_i = \sum_l f_l c_l^i; \quad T = \frac{1}{D} \sum_l f_l |\mathbf{c}_l - \mathbf{u}|^2,$$

we immediately recover that

$$\sum_l f_l^{(n)} = \sum_l c_l^i f_l^{(n)} = \sum_l |\mathbf{c}_l - \mathbf{u}|^2 f_l^{(n)} = 0 \quad n \geq 1. \quad (39)$$

The last equation leads to (we take the convention that double indexes are summed upon)

$$\delta_{ij} \sum_l (c_l^i c_l^j + u_i u_j - u_i c_l^j - u_j c_l^i) f_l^{(n)} = 0 \quad n \geq 1$$

that, combined with the constraints for the momentum ($\sum_l c_l^i f_l^{(n)} = 0$), is equivalent to

$$\sum_l c_l^2 f_l^{(n)} = 0 \quad n \geq 1. \quad (40)$$

2. First order

We first evaluate and also remind the values of some useful quantities that can be easily obtained knowing the relation between Hermite polynomials and the velocity set (33,34) and also the constraints coming from (39,40):

$$\sum_l c_l^i f_l^{(1)} = 0; \quad \sum_l c_l^i \bar{f}_l^{(1)} = \rho \chi_i$$

$$\sum_l c_l^i c_l^j f_l^{(0)} = \rho u_i u_j + \rho T \delta_{ij}$$

$$\frac{1}{2} \sum_l c_l^2 f_l^{(1)} = 0; \quad \frac{1}{2} \sum_l c_l^2 \bar{f}_l^{(1)} = \rho \chi_i u_i$$

$$\frac{1}{2} \sum_l c_l^i c_l^2 f_l^{(0)} = \left(\frac{1}{2} \rho u^2 + \frac{D}{2} \rho T \right) u_i + \rho T u_i.$$

With this, using the momenta of $\mathcal{O}(\epsilon)$ in (38), we can easily arrive to the following set of equations

$$\begin{cases} \partial_{1t} \rho + \partial_i (\rho u_i) = 0 \\ \partial_{1t} (\rho u_i) + \partial_j (\rho u_i u_j + \rho T \delta_{ij}) = \frac{\chi_i}{\tau} = g_i \\ \partial_{1t} \mathcal{K} + \partial_j [\mathcal{K} u_j + \rho T u_j] = \frac{1}{\tau} \rho \chi_i u_i = \rho g_i u_i \end{cases} \quad (41)$$

where we have introduced the total energy of the system:

$$\mathcal{K} = \left(\frac{1}{2} \rho u^2 + \frac{D}{2} \rho T \right)$$

and where we have recovered the Euler equations for a forced fluid with the choice

$$\chi = \tau g. \quad (42)$$

The last equation can also be written as an equation for the temperature (using the momentum equation) in the following form

$$(\partial_{1t} + u_j \partial_j) T + \frac{1}{c_v} T (\partial_i u_i) = 0; \quad c_v = \frac{D}{2}. \quad (43)$$

3. Second Order

Using the second of (38) and the constraints found at the first order it is easy to derive:

$$\sum_l c_l^i (\partial_{1t} f_l^{(0)} + c_l^k \partial_k f_l^{(0)}) = -\frac{1}{\tau} \sum_l c_l^i (f_l^{(1)} - \bar{f}_l^{(1)}) = \rho g_i. \quad (44)$$

Furthermore, let us write other useful quantities that can be derived from the explicit expression of the expansion of the equilibrium distribution, \bar{f}_l , and from the hydrodynamical constraints on the distribution f_l reported in (39) and (40):

$$\sum_l c_l^i c_l^j c_l^k f_l^{(0)} = (\rho u_i u_j u_k + \rho T (\delta_{ij} u_k + \delta_{ik} u_j + \delta_{jk} u_i)) \quad (45)$$

$$\sum_l c_l^i \bar{f}_l^{(2)} = 0; \quad \sum_l c_l^i f_l^{(2)} = 0 \quad (46)$$

$$\frac{1}{2} \sum_l c_l^2 c_l^i \bar{f}_l^{(1)} = \frac{\rho u^2 \chi_i}{2} + u_i \rho \chi_j u_j + \rho T \chi_i + \frac{D \rho T \chi_i}{2} \quad (47)$$

$$\begin{aligned} \frac{1}{2} \sum_l c_l^2 c_l^i c_l^j \bar{f}_l^{(0)} &= \frac{1}{2} \rho u_i u_j u^2 + \frac{\rho T}{2} \delta_{ij} u^2 + \\ 2 \rho T u_i u_j + \frac{1}{2} D \rho T u_i u_j + \left(\frac{D}{2} + 1 \right) \rho T^2 \delta_{ij} \end{aligned} \quad (48)$$

$$\frac{1}{2} \sum_l c_l^2 \bar{f}_l^{(2)} = \frac{1}{2} \rho \chi^2 + \frac{1}{2} D \rho \lambda. \quad (49)$$

We next proceed to evaluate some expressions in terms of the known results obtained at the previous order. In particular, for the momentum equation, we will have to evaluate the term:

$$\partial_{1t} \left(\sum_l c_l^i c_l^j f_l^{(0)} \right) = \partial_{1t} (\rho u_i u_j + \rho T \delta_{ij}).$$

If we use the results obtained at order $\mathcal{O}(\epsilon)$ in (41) we obtain

$$\begin{aligned} \partial_{1t} (\rho u_i u_j + \rho T \delta_{ij}) &= -\partial_k (\rho u_i u_j u_k) - u_j \partial_i (\rho T) - \\ u_i \partial_j (\rho T) + \rho u_j g_i + \rho u_i g_j + \delta_{ij} \rho \partial_{1t} T + \delta_{ij} T \partial_{1t} \rho. \end{aligned} \quad (50)$$

Next, for the momentum equation, we also have to consider

$$\begin{aligned} \partial_{1t} \left(\sum_l c_l^i c_l^j f_l^{(0)} \right) + \partial_k \left(\sum_l c_l^i c_l^j c_l^k f_l^{(0)} \right) &= \\ \partial_{1t} (\rho u_i u_j + \rho T \delta_{ij}) + \partial_k [\rho u_i u_j u_k + \\ \rho T (\delta_{ij} u_k + \delta_{ik} u_j + \delta_{jk} u_i)] \end{aligned}$$

that can be simplified (with results of the previous order) as

$$\begin{aligned} &\partial_{1t} (\rho u_i u_j + \rho T \delta_{ij}) + \\ &+ \partial_k [\rho u_i u_j u_k + \rho T (\delta_{ij} u_k + \delta_{ik} u_j + \delta_{jk} u_i)] = \\ &\rho T \partial_i u_j + \rho T \partial_j u_i + \rho u_j g_i + \rho u_i g_j - \delta_{ij} \frac{\rho T}{c_v} (\partial_k u_k). \end{aligned} \quad (51)$$

For the energy equation we will have to consider

$$\partial_{1t} \left(\sum_l \frac{c_l^2}{2} c_l^i f_l^{(0)} \right) = \partial_{1t} \left[\left(\frac{1}{2} \rho u^2 + \frac{D}{2} \rho T \right) u_i + \rho T u_i \right]$$

that, again, can be evaluated using the results at previous order as

$$\begin{aligned}
\partial_{1t} \left[\left(\frac{1}{2} \rho u^2 + \frac{D}{2} \rho T \right) u_i + \rho T u_i \right] &= \rho (g_k u_k) u_i + \rho T g_i \\
&+ \left(\frac{1}{2} \rho u^2 + \frac{D}{2} \rho T \right) g_i - \partial_j \left[u_i u_j \left(\frac{1}{2} \rho u^2 + \frac{D}{2} \rho T \right) \right] \\
&- 2 \partial_k (\rho T u_i u_k) - \partial_i \left(\frac{1}{2} \rho T u^2 \right) + \rho T u_j \partial_i u_j \\
&- \left(\frac{D}{2} + 1 \right) T \partial_i (\rho T) - \frac{1}{c_v} \rho T u_i (\partial_k u_k) + \rho u_i \partial_j u_j.
\end{aligned} \tag{52}$$

Finally, we have to consider

$$\begin{aligned}
&\partial_{1t} \left(\sum_l \frac{c_l^2}{2} c_l^i f_l^{(0)} \right) + \partial_j \left(\sum_l \frac{c_l^2}{2} c_l^i c_l^j f_l^{(0)} \right) \\
&= \partial_{1t} \left[\left(\frac{1}{2} \rho u^2 + \frac{D}{2} \rho T \right) u_i + \rho T u_i \right] \\
&+ \partial_j \left[\frac{1}{2} \rho u_i u_j u^2 + \frac{\rho T}{2} \delta_{ij} u^2 + 2 \rho T u_i u_j \right] \\
&+ \partial_j \left[\frac{1}{2} D \rho T u_i u_j + \left(\frac{D}{2} + 1 \right) \rho T^2 \delta_{ij} \right]
\end{aligned}$$

that gives

$$\begin{aligned}
&\partial_{1t} \left(\sum_l \frac{c_l^2}{2} c_l^i f_l^{(0)} \right) + \partial_j \left(\sum_l \frac{c_l^2}{2} c_l^i c_l^j f_l^{(0)} \right) = \\
&+ \rho (g_k u_k) u_i + \rho T g_i + \left(\frac{1}{2} \rho u^2 + \frac{D}{2} \rho T \right) g_i + \\
&\left(\frac{D}{2} + 1 \right) \rho T \partial_i T + \rho T (u_i \partial_j u_j + u_j \partial_i u_j) - \\
&- \frac{1}{c_v} \rho T u_i (\partial_k u_k).
\end{aligned} \tag{53}$$

We are now ready to write down the equations at this order using results in (45)-(48) and (50)-(53)

$$\left\{ \begin{aligned}
&\partial_{2t} \rho + 1/2 \partial_i (\rho g_i \Delta t) = 0 \\
&\partial_{2t} (\rho u_i) + \partial_j (\tau \rho g_i u_j + \tau \rho g_j u_i) + \partial_{1t} \left(\frac{\rho g_i}{2} \Delta t \right) = \\
&\left(\tau - \frac{\Delta t}{2} \right) \partial_j (\rho T \partial_i u_j + \rho T \partial_j u_i + \rho u_j g_i + \rho u_i g_j \\
&- \delta_{ij} \frac{\rho T}{c_v} (\partial_k u_k)) \\
&\partial_{2t} \mathcal{K} + \partial_k [\mathcal{K} \tau g_k + \tau \rho u_k g_k + \rho T g_k] + \partial_{1t} \left(\frac{\rho g_i u_i}{2} \Delta t \right) - \\
&\left(\tau - \frac{\Delta t}{2} \right) \partial_i [\rho (g_k u_k) u_i + \rho T g_i + \mathcal{K} g_i + \left(\frac{D}{2} + 1 \right) \rho T \partial_i T \\
&+ \rho T u_i \partial_j u_j + \rho T u_j \partial_i u_j - \frac{1}{c_v} \rho T u_i (\partial_k u_k)] = \\
&= \frac{1}{\tau} \left(\frac{1}{2} \rho \tau^2 g^2 + \frac{1}{2} D \rho \lambda \right).
\end{aligned} \right.$$

Summing up all orders, we note that we can *freely* add at order $\mathcal{O}(\epsilon^2)$ all the gradients of terms $\mathcal{O}(g^2)$ and also double gradients of terms $\mathcal{O}(g)$ because they would be $\mathcal{O}(\epsilon^3)$. Also, defining the hydrodynamic velocity as $u_i^{(H)} = u_i + \frac{g_i \Delta t}{2}$,

we reconstruct the following equation s:

$$\begin{cases} \partial_t \rho + \partial_i(\rho u_i^{(H)}) = 0 \\ \partial_t(\rho u_i^{(H)}) + \partial_j(\rho u_i^{(H)} u_j^{(H)}) = -\partial_i(\rho T) + g_i \\ + \left(\tau - \frac{\Delta t}{2}\right) \partial_j \left[\rho T \partial_i u_j^{(H)} + \rho T \partial_j u_i^{(H)} - \delta_{ij} \frac{\rho T}{c_v} \partial_k u_k^{(H)} \right] \\ \partial_t \mathcal{K}^{(H)} + \partial_j \left[\mathcal{K}^{(H)} u_j^{(H)} + \rho T u_j^{(H)} \right] = \rho g_k u_k + \\ \frac{1}{2\tau} (\rho \tau^2 g^2 + D \rho \lambda) + \left(\tau - \frac{\Delta t}{2}\right) \partial_i \left[\left(\frac{1}{2} D + 1\right) \rho T \partial_i T + \right. \\ \left. \rho T u_i^{(H)} \partial_j u_j^{(H)} + \rho T u_j^{(H)} \partial_i u_j^{(H)} - \frac{1}{c_v} \rho u_i^{(H)} (\partial_k u_k^{(H)}) \right] \end{cases}$$

with

$$\mathcal{K}^{(H)} = \left(\frac{1}{2} \rho (u^{(H)})^2 + \frac{D}{2} \rho T \right).$$

In order to recover the correct thermohydrodynamical evolution we need to obtain the correct forcing in the equation for the total energy in terms of the hydrodynamical velocity fields, i.e.

$$\rho g_k u_k + \frac{1}{2\tau} (\rho \tau^2 g^2 + D \rho \lambda) = \rho g_k u_k^{(H)} = \rho g_k \left(u_k + \frac{\Delta t g_k}{2} \right)$$

that leads to

$$\lambda = \frac{\tau(\Delta t - \tau)g^2}{D}. \quad (54)$$

In conclusions, expressing everything in terms of the hydrodynamical fields, it is easy to realize that the final expression (54) coincides with the one given in the body of the article (9). Notice that up to now we have used a single-time relaxation LBM, as given by (32). Therefore, the final Fourier-Navier-Stokes equations are constrained to describe fluids with unit Prandtl numbers, $Pr = \nu/(k/c_p) = 1$. It is possible to generalize the approach by using a multi-relaxation time version of the same algorithm [29]. Even though, in the latter case, there exists a small mismatch in the viscous dissipation term appearing in the energy balance.

VII. APPENDIX B

In this appendix we detail the technical steps leading to the desired hydrodynamical boundary conditions for the physical systems analyzed in the paper, i.e. an ideal gas under the effect of gravity $\mathbf{g} = (0, -g)$ acting along the negative z direction (i.e. g is positive). Similar ideas can be applied to the case of a generic volume or internal force acting also in the stream-wise x direction. For the sake of concreteness we explicitly report the case of the lower boundary condition with the upper boundary condition being a straightforward generalization. Let us call the post streaming populations f_l^* while keeping $f_l^{(*,pre)}$ to identify the pre streaming populations. Moreover, all the populations will also undergo collisions and therefore there will be a net gain of momentum so that the hydrodynamic fields will be the average of pre and post collisions. For a given computational boundary, there are 3 layers of points labeled by \mathbf{x}^* from now on (see also figure 13), where some unknown populations have to be set soon after the streaming step. We use the freedom to set these populations in such a way that the measured hydrodynamic quantities such as the stream-wise ($u_x^{(H)}$) and vertical ($u_z^{(H)}$) velocity and also the temperature ($T^{(H)}$) are fixed to some given boundary conditions on those lattice layers. The conditions to be fulfilled up to the second order in the Chapman-Enskog expansion (see also previous appendix) are

$$u_x^{(H)}(\mathbf{x}^*) = \frac{1}{\rho(\mathbf{x}^*)} \sum_l f_l^*(\mathbf{x}^*) c_l^x \quad (55)$$

$$u_z^{(H)}(\mathbf{x}^*) = \frac{1}{\rho(\mathbf{x}^*)} \sum_l f_l^*(\mathbf{x}^*) c_l^z - \frac{\Delta t}{2} g \quad (56)$$

$$\begin{aligned} \frac{D}{2}T^{(H)}(\mathbf{x}^*) + \frac{1}{2}((u^{(H)})^2 + (v^{(H)})^2)(\mathbf{x}^*) &= \\ &= \frac{1}{2\rho(\mathbf{x}^*)} \sum_l f_l^*(\mathbf{x}^*) c_l^2. \end{aligned} \quad (57)$$

In the following we show how to determine the unknown populations on the first three layers (those coming –after streaming– from node outside the domain) in order to set the vertical velocity to zero on layer 3, with any temperature and stream-wise velocities:

$$\begin{cases} u_z^{(H)}(z=3) = 0 \\ u_x^{(H)}(z=3) = u_3 \\ T^{(H)}(z=3) = T_3. \end{cases}$$

Similarly we can fix any desired profile for temperature and velocity on layers 1, 2:

$$\begin{cases} u_z^{(H)}(z=2) = v_2; & u_z^{(H)}(z=1) = v_1 \\ u_x^{(H)}(z=2) = u_2; & u_x^{(H)}(z=1) = u_1 \\ T^{(H)}(z=2) = T_2; & T^{(H)}(z=1) = T_1. \end{cases}$$

We will define only the case of homogeneous boundary conditions along the stream-wise component but the method is general and can deal also non-homogeneous cases. Imposing a given set of boundary conditions means defining the set of *unknown* outgoing populations in the first three layers in terms of the set of in-going and outgoing *known* populations such that mass is conserved and the hydrodynamical fields defined above are the wanted ones.

In this way, if the computational boundary extends from the mesh point $z = 1$ up to $z = L_z$, the real physical domain is between mesh points $z = 3$ and $z = L_z - 2$, i.e. it is in these points that we exactly verify the condition of no-slip, no normal velocity and given temperature for the hydrodynamical fields on the solid walls. Fields at points $z = 1, 2$ and $z = L_z - 1, L_z - 2$ may be used to better stabilize the algorithm close to the boundaries. All details refer to the 37 speed model *D2Q37*.

Layer 1

As evident from figure 13 we have to determine some 'outer' post streaming populations ($l = 2, 10, 18, \dots$) whereas other post streaming populations ($l = 4, 12, 20, \dots$) are known. To keep a compact notation, let us also introduce the subsets $I^{(1)}, U^{(1)}$ and $I_0^{(1)}$ which are identified by the following conditions

$$I^{(1)} = \{\mathbf{c}_l, c_l^z < 0\}; \quad U^{(1)} = \{\mathbf{c}_l, c_l^z > 0\}$$

$$I_0^{(1)} = \{\mathbf{c}_l, c_l^z \leq 0\}.$$

We choose to define the 'outer' populations in the layer 1 as

$$f_l^{(1,*)} = \frac{N}{\sum_{l \in U^{(1)}} \phi_l^{(1)}} \phi_l^{(1)} \quad l \in U^{(1)} \quad (58)$$

with N a constant and $\phi_l^{(1)}$ a suitable population that we choose in the form

$$\phi_l^{(1)} = 1 + \mathbf{c}_l \cdot \mathbf{p}^{(1)} + \frac{1}{2} c_l^2 E^{(1)} \quad (59)$$

where $p_x^{(1)}, p_z^{(1)}$ and $E^{(1)}$ are unknown at this level and must be chosen in such a way that the hydrodynamical temperature and momentum *exactly* reproduce the desired values on this layer, T_1, u_1, v_1 . Also, mass conservation should be fulfilled. This latter condition is naturally imposed by setting

$$N = \sum_{l \in I^{(1)}} f_l^{(1,*,pre)}.$$

The requirement that T_1, u_1, v_1 are exactly reproduced leads to the following system of equations

$$\begin{cases} u_1 = \frac{1}{M_p} \sum_l f_l^* c_l^x \\ v_1 = \frac{1}{M_p} \sum_l f_l^* c_l^z - \frac{\Delta t}{2} g \\ T_1 = \frac{1}{M_p D} \sum_l f_l^* c_l^2 + \frac{1}{D} (u_1^2 + v_1^2) \end{cases} \quad (60)$$

where we have defined the post streaming mass as

$$M_p = N + \sum_{l \in I_0^{(1)}} f_l^{(1,*)}.$$

In the $\sum_l f_l^*$ of system (60) we have known populations coming from the bulk but also 'outer' populations to be determined with (58) and (59). The resulting system is therefore an algebraic system for $p_x^{(1)}, p_z^{(1)}$ and $E^{(1)}$. We have solved the system whose final solution is

$$\begin{aligned} p_z^{(1)} &= \frac{-c_3 d_2 + c_2 d_3}{-a_3 c_2 + a_2 c_3} \\ p_x^{(1)} &= \frac{a_2 c_3 d_1 - a_2 c_1 d_3 - a_3 c_2 d_1 - c_3 a_1 d_2 + c_1 a_3 d_2 + a_1 c_2 d_3}{b_1 (a_3 c_2 - a_2 c_3)} \\ E^{(1)} &= \frac{-a_3 d_2 + a_2 d_3}{a_3 c_2 - a_2 c_3} \end{aligned}$$

where

$$\begin{aligned} a_1 &= 26(\tilde{p}_x - O_x)r; & b_1 &= -40Nr^2 \\ c_1 &= 47(\tilde{p}_x - O_x)r^2; & d_1 &= 15(\tilde{p}_x - O_x) \\ a_2 &= 26(\tilde{p}_z - O_z)r - 54Nr^2; & c_2 &= 47(\tilde{p}_z - O_z)r^2 - 91Nr^3 \\ d_2 &= 15(\tilde{p}_z - O_z) - 26Nr; & a_3 &= 26(\tilde{E} - O_e)r - 91Nr^3 \\ c_3 &= 47(\tilde{E} - O_e)r^2 - \frac{367}{2}Nr^4; & d_3 &= 15(\tilde{E} - O_e) - 47Nr^2 \end{aligned}$$

with

$$\tilde{p}_x^{(1)} = M_p u_1; \quad \tilde{p}_z^{(1)} = M_p v_1 + \frac{1}{2} M_p g \Delta t$$

$$\tilde{E} = T_1 M_p + \frac{1}{2M_p} ((\tilde{p}_x^{(1)})^2 + (\tilde{p}_z^{(1)})^2)$$

and

$$O_x = \sum_{l \in I_0^{(1)}} c_l^x f_l^{(1,*)}; \quad O_z = \sum_{l \in I_0^{(1)}} c_l^z f_l^{(1,*)}$$

$$O_e = \sum_{l \in I_0^{(1)}} \frac{1}{2} c_l^2 f_l^{(1,*)}.$$

In the above r is the lattice constant whose value for the $D2Q37$ model is $r \sim 1.1969$ [29].

Layer 2

Situation goes similarly with respect to the previous layer. We new have to define the subsets $I^{(2)}, U^{(2)}$ and $I_0^{(2)}$ as

$$I^{(2)} = \{\mathbf{c}_l, c_l^z < -r\}; \quad U^{(2)} = \{\mathbf{c}_l, c_l^z > r\}$$

$$I_0^{(2)} = \{\mathbf{c}_l, c_l^z \leq r\}.$$

We then identify some coarse grained quantities as

$$N = \sum_{l \in I^{(2)}} f_l^{(2,*)}; \quad M_p = N + \sum_{l \in I_0^{(2)}} f_l^{(2,*)}$$

ad define some local momentum and energy fields

$$\tilde{p}_x^{(2)} = M_p u_2$$

$$\tilde{p}_z^{(2)} = M_p v_2 + \frac{1}{2} M_p g \Delta t$$

$$\tilde{E}^{(2)} = T_2 M_p + \frac{1}{2 M_p} ((\tilde{p}_x^{(2)})^2 + (\tilde{p}_z^{(2)})^2).$$

We next define

$$O_x = \sum_{l \in I_0^{(2)}} c_l^x f_l^{(2,*)}; \quad O_z = \sum_{l \in I_0^{(2)}} c_l^z f_l^{(2,*)}$$

$$O_e = \sum_{l \in I_0^{(2)}} \frac{1}{2} c_l^2 f_l^{(2,*)}$$

$$a_1 = 19(\tilde{p}_x - O_x)r; \quad b_1 = -12Nr^2$$

$$c_1 = \frac{59}{2}(\tilde{p}_x - O_x)r^2; \quad d_1 = 8(\tilde{p}_x - O_x)$$

$$a_2 = 19(\tilde{p}_z - O_z)r - 47Nr^2; \quad c_2 = \frac{59}{2}(\tilde{p}_z - O_z)r^2 - \frac{147}{2}Nr^3$$

$$d_2 = 8(\tilde{p}_z - O_z) - 19Nr; \quad a_3 = 19(\tilde{E} - O_e)r - \frac{147}{2}Nr^3$$

$$c_3 = \frac{59}{2}(\tilde{E} - O_e)r^2 - \frac{475}{4}Nr^4; \quad d_3 = 8(\tilde{E} - O_e) - \frac{59}{2}Nr^2.$$

In terms of these constants and parameters we can set

$$p_z^{(2)} = \frac{-c_3 d_2 + c_2 d_3}{-a_3 c_2 + a_2 c_3}$$

$$p_x^{(2)} = \frac{a_2 c_3 d_1 - a_2 c_1 d_3 - a_3 c_2 d_1 - c_3 a_1 d_2 + c_1 a_3 d_2 + a_1 c_2 d_3}{b_1(a_3 c_2 - a_2 c_3)}$$

$$E^{(2)} = \frac{-a_3 d_2 + a_2 d_3}{a_3 c_2 - a_2 c_3},$$

construct suitable populations

$$\phi_l^{(2)} = 1 + \mathbf{c}_l \cdot \mathbf{p}^{(2)} + \frac{1}{2} c_l^2 E^{(2)}$$

and define the outer populations in the layer 2 as

$$f_l^{(2,*)} = \frac{N}{\sum_{l \in U^{(2)}} \phi_l^{(2)}} \phi_l^{(2)} \quad l \in U^{(2)}$$

that is enough to set the hydrodynamic velocity to u_2 and v_2 while keeping the hydrodynamic temperature to T_2 .

Layer 3

As also evident from the figure 13, only 3 populations are unknown on the third layer (they are populations $l = 24, 25, 18$). In this way we do not have enough freedom to choose the desired hydrodynamic velocities and temperature. It is anyhow possible to require a zero vertical hydrodynamic velocity ($v_3 = 0$) with a generic stream-wise hydrodynamic velocity and temperature (u_3, T_3). Again, let us introduce the following sets

$$U^{(3)} = \{c_l, c_l^z > 2r\}; \quad I_0^{(3)} = \{c_l, c_l^z \leq 2r\}.$$

The boundary condition for the unknown populations is set as

$$f_l^{(3,*)} = \frac{N}{\sum_{l \in U^{(3)}} \phi_l^{(3)}} \phi_l^{(3)} \quad l \in U^{(3)}$$

$$\phi_l^{(3)} = 1 + c_l^x p_x^{(3)} + \frac{1}{2} c_l^2 E^{(3)}$$

and we choose $p_x^{(3)}$ and $E^{(3)}$ to set the desired hydrodynamical stream-wise velocity (u_3) and temperature (T_3) while keeping the vertical hydrodynamical velocity to zero. The resulting algebraic system is solved with the solution

$$E^{(3)} = -\frac{d_2}{b_2}; \quad p_x^{(3)} = \frac{b_1 d_2 - d_1 b_2}{a_1 b_2}$$

with

$$a_1 = -2Nr^2; \quad b_1 = \frac{29}{2}(\tilde{p}_x - O_x)r^2$$

$$d_1 = 3(\tilde{p}_x - O_x); \quad b_2 = \frac{29}{2}(\tilde{E} - O_e)r^2 - \frac{281}{4}Nr^4$$

$$d_2 = 3(\tilde{E} - O_e) - \frac{29}{2}Nr^2$$

where

$$O_x = \sum_{l \in I_0^{(3)}} c_l^x f_l^{(3,*)}; \quad O_e = \sum_{l \in I_0^{(3)}} \frac{1}{2} c_l^2 f_l^{(3,*)}$$

$$\tilde{p}_x^{(3)} = M_p u_3$$

$$\tilde{E}^{(3)} = T_3 M_p + \frac{1}{2M_p}((\tilde{p}_x^{(3)})^2 + (\tilde{p}_z^{(3)})^2)$$

$$\tilde{p}_z^{(3)} = 3Nr + \sum_{l \in I_3^{(0)}} c_l^z f_l^{(3,*)}$$

$$M_p = N + \sum_{l \in I_0^{(3)}} f_l^{(3,*)}.$$

$$N = -\frac{A_1}{3r} + \frac{1}{2} \frac{A_2}{3r} g \Delta t$$

$$A_1 = \sum_{l \in I_3^{(0)}} c_l^z f_l^{(3,*)}; \quad A_2 = \sum_{l \in I_3^{(0)}} f_l^{(3,*)} - f_0^{(3,*)}. \quad (61)$$

This whole algorithm for layer 3 now is ensuring a zero vertical hydrodynamical velocity and arbitrary u_3 and T_3 . Still, mass conservation is not fulfilled and to do that we need to redefine the rest population appearing in (61) as

$$f_0^{(3,*)} = f_0^{(3,*,pre)} - N + \sum_{l, c_l^z = -3r} f_l^{(3,*)}.$$

-
- [1] X. Shan X. & H. Chen. Lattice Boltzmann model for simulating flows with multiple phases and components. *Phys. Rev E* **47**, 1815 (1993)
 - [2] M.R. Swift, W.R. Osborn & J.M. Yeomans. Lattice Boltzmann Simulation of Nonideal Fluids. *Phys. Rev. Lett.* **75**, 830 (1995)
 - [3] Q. Li & A.J. Wagner. Symmetric free-energy-based multicomponent lattice Boltzmann method. *Phys. Rev. E* **76**, 036701 (2007)
 - [4] X. He X. & L.S. Luo. Theory of the Lattice Boltzmann Method: from the Boltzmann equation to the Lattice Boltzmann equation. *Phys. Rev. E* **56**, 6811 (1997)
 - [5] A.J.C. Ladd. Numerical simulations of particulate suspensions via a discretized Boltzmann equation. 2. Numerical Results. *J. Fluid. Mech.* **271**, 311 (1994)
 - [6] J. Harting, C. Kunert & J. Hyvaluoma. Lattice Boltzmann simulations in microfluidics: probing the no-slip boundary condition in hydrophobic, rough, and surface nanobubble laden microchannels. *Microfluidics and Nanofluidics* **8**, 1 (2009)
 - [7] B. Duenweg & A. J. C. Ladd. Lattice Boltzmann simulations of soft matter systems. *Adv. Poly. Sci.* **221**, 89-166 (2009)
 - [8] R. R. Nourgaliev, T. N. Dinh, T. G. Theofanous & D. Joseph. The Lattice Boltzmann equation method: theoretical interpretation, numerics and implications. *Int. J. Multiphase Flow* **29**, 117 (2003)
 - [9] D. Wolf-Gladrow. *Lattice-Gas Cellular Automata And Lattice Boltzmann Models*. Springer, New York (2000)
 - [10] R. Benzi, S. Succi & M. Vergassola. The lattice Boltzmann equation: theory and applications. *Phys. Rep.* **222**, 145 (1992)
 - [11] S. Chen & G. Doolen. Lattice Boltzmann method for fluid flows. *Annu. Rev. Fluid Mech.* **30**, 329 (1998)
 - [12] P.-L. Bathnagar, E. Gross & M. Krook. A model for collision processes in gases. *Physical review* **94**, 511 (1954)
 - [13] X. Shan & X. He. Discretization of the Velocity Space in the Solution of the Boltzmann Equation. *Phys. Rev. Lett.* **80**, 65 (1998)
 - [14] N.S. Martys, X. Shan & H. Chen. Evaluation of the extrenal force term in the discrete Boltzmann equation. *Phys. Rev. E* **58**, 6865 (1998)
 - [15] X. Shan, F. Yuan & H. Chen. Kinetic theory representation of hydrodynamics: a way beyond the NavierStokes equation. *Jour. Fluid Mech.* **550**, 413 (2006)
 - [16] X. He & G. Doolen. Thermodynamic Foundations of Kinetic Theory and Lattice Boltzmann Models for Multiphase Flows. *Jour. Stat. Physics* **107**, 309 (2001)
 - [17] R. Benzi, L. Biferale, M. Sbragaglia, S. Succi & F. Toschi. Mesoscopic Modelling of a Two-Phase Flow in Presence of the Boundaries: the Contact Angle. *Phys. Rev. E* **74**, 021509 (2006)
 - [18] M. Sbragaglia, R. Benzi, L. Biferale, S. Succi & F. Toschi. Surface roughness-hydrophobicity coupling in microchannel and nanochannel flows. *Phys. Rev. Lett.* **97**, 204503 (2006)
 - [19] J. Hyvaluoma & J. Harting. Slip flow over structured surfaces with entrapped microbubbles. *Phys. Rev. Lett.* **100**, 246001 (2008)
 - [20] P. Lallemand & L. S. Luo. Theory of the lattice Boltzmann method: Acoustic and thermal properties in two and three dimensions. *Phys. Rev. E* **68**, 036706 (2003)
 - [21] N.I. Prasianakis, I.V. Karlin, J. Mantzaras & K.B. Boulouchos. Lattice Boltzmann method with restored Galilean invariance. *Phys. Rev. E* **79**, 066702 (2009)
 - [22] N.I. Prasianakis & I.V. Karlin. Lattice Boltzmann method for thermal flow simulation on standard lattices. *Phys. Rev. E* **76**, 016702 (2007)
 - [23] V. Sofonea. Implementation of diffuse reflection boundary conditions in a thermal lattice Boltzmann model with flux limiters. *Jour. Comp. Phys.* **228**, 6107 (2009)
 - [24] G. Gonnella A. Lamura & V. Sofonea. Lattice Boltzmann simulation of thermal nonideal fluids. *Phys. Rev. E* **76**, 036703 (2007)
 - [25] M. Watari. Velocity slip and temperature jump simulations by the three-dimensional thermal finite-difference lattice Boltzmann method. *Phys. Rev. E* **79**, 066706 (2009)
 - [26] P.C. Philippi et al. From the continuous to the lattice Boltzmann equation: The discretization problem and thermal models. *Phys. Rev. E* **73**, 056702 (2006)
 - [27] X. Nie, X. Shan & H. Chen. Thermal lattice Boltzmann model for gases with internal degrees of freedom. *Phys. Rev. E* **77**, 035701(R) (2008)
 - [28] J. Meng and Y. Zhang. Accuracy Analysis of high-order lattice Boltzmann models for rarified gas flows. *arXiv:0908.4520v2* (2009)
 - [29] X. Shan & H. Chen. A general multi-relaxation-time Boltzmann collision model. *Int. Jour. of Modern Physics C* **18**, 635-643 (2007)
 - [30] R. Surmas, C.E. Pico Ortiz & P.C. Philippi. Simulating thermohydrodynamics by finite difference solutions of the Boltzmann equations. *Eur. Phys. J. Special Topics* **171**, 81-90 (2009)
 - [31] S. Ansumali & I. Karlin. Kinetic boundary conditions in the lattice Boltzmann method. *Phys. Rev. E* **66**, 026311 (2002)
 - [32] D. N. Siebert, L. A. Hegele, & P. C. Philippi. Lattice Boltzmann equation linear stability analysis: Thermal and athermal models. *Phys. Rev. E* **77**, 026707 (2008)
 - [33] M. Sbragaglia et al. Lattice Boltzmann method with self-consistent thermo-hydrodynamic equilibria. *J. Fluid Mech.* **628**, 299 (2009)
 - [34] E.A. Spiegel. Convective instability in a comprssible atmosphere. *Astrophys. J.* **141**, 1068 (1965)

- [35] E.A. Spiegel & G. Veronis. On the Boussinesq approximation for a compressible fluid. *Astrophys. J.* **131**, 442 (1960)
- [36] G. Ahlers, S. Grossmann & D. Lohse. Heat transfer and large-scale dynamics in turbulent Rayleigh-Benard convection. *Rev Mod. Phys.* **81**, 503-537 (2009)
- [37] J.M. Buick & C.A. Greated. Gravity in a lattice Boltzmann model. *Phys. Rev E* **61**, 5307 (2000)
- [38] Z. Guo, C. Zheng & B. Shi. Discrete lattice effects on the forcing term in the lattice Boltzmann method, *Phys. Rev. E* **65**, 046308 (2002)
- [39] A. Celani, A. Mazzino, P. Muratore-Ginanneschi and L. Vozella. Phase-field model for the Rayleigh-Taylor instability of immiscible fluids. *J. Fluid Mech* **622**, 115-134 (2009)
- [40] D.N. Siebert, L.A. Hegele, R. Surmas, L.O. Emerich Dos Santos & P.C. Philippi. Thermal Lattice Boltzmann in two dimensions. *Int. Jour. of Modern Physics C* **18**, 546 (2007)
- [41] J. Frolich & S. Gauthier. Numerical investigations from compressible to isobaric Rayleigh-Benard convection in two dimensions. *Eur. J. Mech. B/Fluids* **12** 141 (1993)
- [42] F. Robinson & K. Chan. Non-Boussinesq simulations of Rayleigh-Benard convection in a perfect gas. *Phys. Fluids* **16** 1321 (2004)
- [43] Notice that this can be exactly implemented in the LBM by redefining the relaxation time at each iteration such as $(\tau - \Delta t)/2 = \text{const.}/(T^{(H)}\rho)$
- [44] L.D. Landau & E.M. Lifshitz. *Fluid Mechanics*. Pergamon Press.
- [45] J. Thomas, N. Weiss & S. Tobias. Downward pumping of magnetic flux as the cause of filamentary structures in sunspot penumbrae. *Nature* **420** 390 (2002)
- [46] N.H. Brummell. Turbulent compressible convection with rotation. *Proceedings of the International Astronomical Union* **2**, 417 (2006)
- [47] G. Ahlers, F. F. Araujo, D. Funfschilling, S. Grossmann & D. Lohse. Non-Oberbeck-Boussinesq Effects in Gaseous Rayleigh-Benard Convection. *Phys. Rev. Letters* **98**, 054501 (2007)
- [48] G. Ahlers, B. Dressel, J. Oh & W. Pesch. Strong non-Boussinesq effects near the onset of convection in a fluid near its critical point. *J. Fluid. Mech.*, to appear (2009)
- [49] J.Zhang, X.L. Wu & K-Q Xia. Density fluctuations in strongly stratified two-dimensional turbulence. *Phys. Rev. Lett.* **94** 174503. (2005)
- [50] S. Chandrasekhar. *Hydrodynamic and Hydromagnetic Stability*. Oxford Clarendon Press.
- [51] D.O. Gough, D.R Moore, E.A. Spiegel & N.O. Weiss. Convective instability in a comprssible atmosphere. II. *Astrophys. J.* **206**, 536 (1976)
- [52] E. Graham. Numerical simulation of two-dimensional compressible convection. *J. Fluid Mech.* **70**, 689 (1975)
- [53] R.J.A.M. Stevens, R. Verzicco & D. Lohse. Radial boundary layer structure and Nusselt number in Rayleigh-Benard convection. *arXiv:0905.0379v1*.
- [54] H. Chen, C. Teixeira & K. Molvig. Realization of fluid boundary conditions via discrete Boltzmann dynamics. *Int. J. Mod. Phys. C* **9** 1281-1292 (1998)
- [55] K. Sugiyama, E. Calzavarini, S. Grossmann & D. Lohse. Non-Oberbeck-Boussinesq effects in two-dimensional Rayleigh-Bnard convection in glycerol. *Europhys. Lett.* **80**, 34002 (2007)
- [56] K. Sugiyama, E. Calzavarini, S. Grossmann & D. Lohse. Flow organization in two-dimensional non-OberbeckBoussinesq Rayleigh-Bénard convection in water. *J. Fluid Mech.* **637**, 105-135 (2009)
- [57] J.D. Lindl. *Inertial Confinement Fusion* (Springer-Verlag, New-York) 1998.
- [58] M. Zingale, S.E. Woosley, C.A. Rendleman, M.S. Day & J.B. Bell. Three-dimensional Numerical Simulations of Rayleigh-Taylor Unstable Flames in Type Ia Supernovae. *Astrophys. J.* **632**, 1021 (2005) .
- [59] D.H. Sharp. An overview of Rayleigh-Taylor instability. *Physica D* **12**, 3 (1084)
- [60] G. Dimonte et al. A comparative study of the Rayleigh-Taylor instability using high-resolution three-dimensional numerical simulations: The Alpha group collaboration. *Phys. Fluids* **16** 1668 (2004)
- [61] D. Livescu et al. High Reynolds numbers Rayleigh-Taylor turbulence. *J. Turbul.* **10** num. 13, 1 (2009)
- [62] G. Boffetta, A. Mazzino, S. Musacchio & L. Vozzella. Kolmogorov scaling and intermittency in Rayleigh-Taylor turbulence. *Phys. Rev E* **79** 065301 (2009)
- [63] M. Chertkov. Phenomenology of Rayleigh-Taylor Turbulence. *Phys. Rev. Lett.* **91** 115001. (2003)
- [64] W. Cabot. Comparison of two- and three-dimensional simulations of miscible Rayleigh-Taylor instability. *Phys Fluids* **18**, 045101 (2006)
- [65] I.B. Bernstein & D. L. Book, Effect of compressibility on the Rayleigh-Taylor instability. *Phys Fluids* **26**, 453 (1983)
- [66] M.-A. Lafay, B. Le Creurer & S. Gauthier. Compressibility effects on the Rayleigh-Taylor instability between miscible fluids. *Europhys. Lett.* **79**, 64002 (2007)
- [67] S. Gauthier, private communication.
- [68] B. Le Creurer & S. Gauthier. A return toward equilibrium in a 2d Rayleigh-Taylor instability for compressible fluids with a multidomain adaptive Chebyshev method. *Theor Comput. Fluid Dyn.* **22**, 125 (2008)
- [69] A. Celani, A. Mazzino & L. Vozella. Rayleigh-Taylor turbulence in two dimensions. *Phys. Rev. Lett.* **96**, 134504. (2006)
- [70] A. Celani, T. Matsumoto, A. Mazzino & M. Vergassola. Scaling and universality in turbulent convection. *Phys. Rev. Lett.* **88**, 054503 (2002)
- [71] J.R. Ristorcelli & T.T. Clark. Rayleigh-Taylor turbulence: self-similar analysis and direct numerical simulations. *J. Fluid Mech.* **507**, 213 (2004)
- [72] W.H. Cabot & A. W. Cook. Reynolds number effects on Rayleigh-Taylor instability with possible implications for type-Ia

- supernovae. *Nature* **2**, 562 (2006)
- [73] T.T. Clark. A numerical study of the statistics of a two dimensional Rayleigh-Taylor mixing layer. *Phys. Fluids* **15**, 2413 (2003)
- [74] H. Grad. On the kinetic theory of rarefied gases. *Pure Appl. Math.* **2**, 325 (1949)
- [75] F. Belletti, L. Biferale, F. Mantovani, S. F. Schifano, F. Toschi & R. Tripiccone. Multiphase Lattice Boltzmann on the Cell Broadband Engine. *Il Nuovo Cimento C* **32** 53 (2009).
- [76] L. Biferale, F. Mantovani, M. Sbragaglia, A. Scagliarini, S. F. Schifano, F. Toschi, R. Tripiccone. High resolution study of compressible Rayleigh-Taylor turbulence. in preparation (2010).

	At	L_x	L_z	L_{ad}	ν	g	T_u	T_d	N_{conf}	$\tilde{\tau}$
run A	0.05	800	2400	4×10^3	0.001	5×10^{-5}	0.95	1.05	50	1.8×10^4
run B	0.4	1664	4400	1.6×10^4	0.1	1×10^{-4}	0.6	1.4	35	6.5×10^3

TABLE I: Parameters for the two sets of Rayleigh-Taylor run. Atwood number, $At = (T_d - T_u)/(T_d + T_u)$; Adiabatic Length, $L_{ad} = (T_d - T_u)c_p/g$ ($c_p = 2$); viscosity ν ; gravity g ; temperature in the upper half region, T_u ; temperature in the lower half region, T_d ; number of separate Rayleigh-Taylor run N_{conf} ; normalization time, $\tilde{\tau} = \sqrt{L_x/(g At)}$ (not to be confused with the relaxation time of the lattice Boltzmann model (2)). Given the parameters here used, the typical resolution obtained is good enough to get an agreement better than a few per cent on the global exact balance between kinetic energy growth and the sum of dissipation plus buoyancy force.

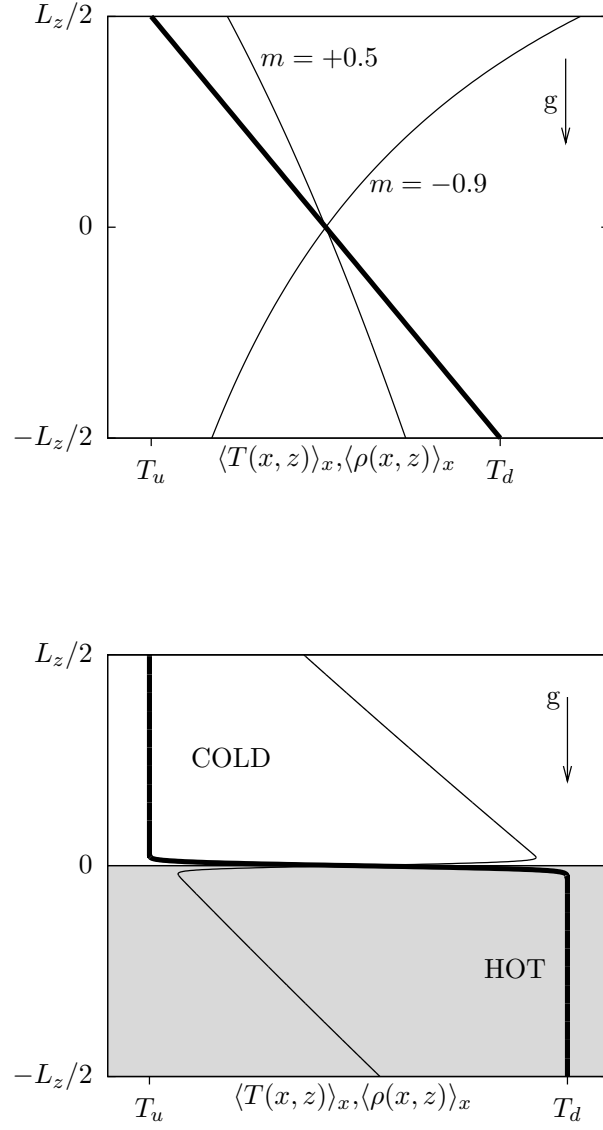


FIG. 1: Upper panel: Rayleigh-Bénard geometry and set-up of the initial configuration given by eq. (14); two cases with $m = +0.5$ and $m = -0.9$. On the horizontal axis we show the mean temperature and density profiles as a function of the z -height (plotted on the vertical axis). The bold and tiny solid lines represent the temperature and density profiles respectively. Lower panel: Rayleigh-Taylor initial configuration given by eq. (17). Bold and tiny lines as in the upper panel.

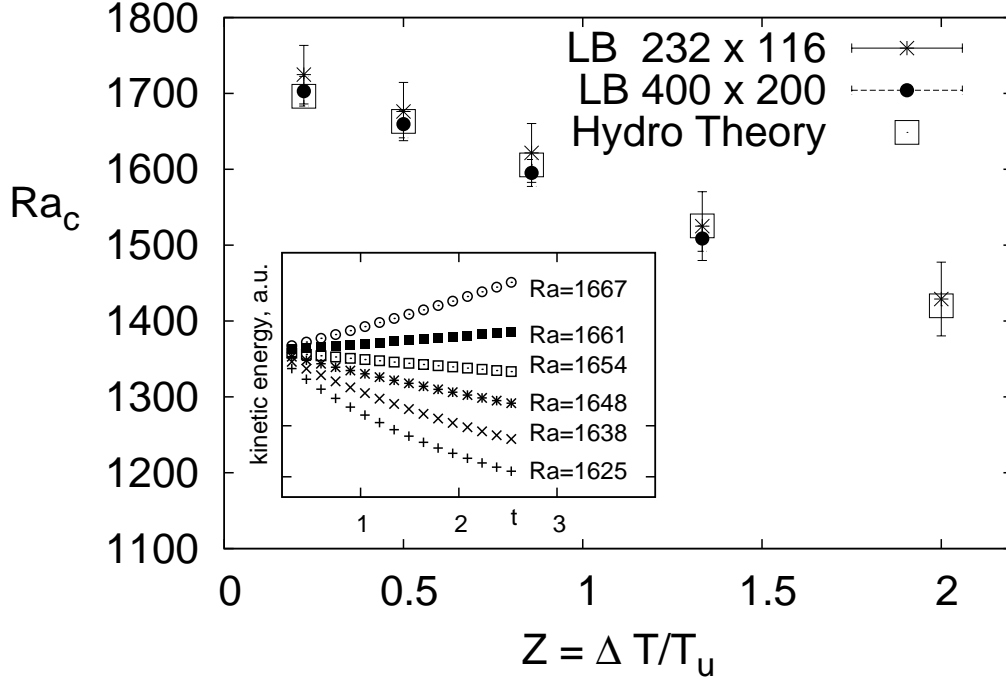


FIG. 2: Critical Rayleigh number, estimated at the center of the cell, \tilde{Ra}_c , at changing the polytropic index, m , the scale height, Z , and the numerical resolutions. For the smallest resolution, $L_x \times L_z = 232 \times 116$, the plotted values corresponds to (a) $Z = 0.22, \Delta T = 0.2, T_d = 0.9, m = -0.942$; (b) $Z = 0.5, \Delta T = 0.4, T_d = 0.8, m = -0.971$; (c) $Z = 0.86, \Delta T = 0.6, T_d = 0.7, m = -0.9806$; (d) $Z = 1.33, \Delta T = 0.8, T_d = 0.6, m = -0.9855$; (e) $Z = 2.0, \Delta T = 1.2, T_d = 0.6, m = -0.990$. Theoretical values are obtained solving the linearized equations as described in [34]. Inset: time evolution of the total kinetic energy (in arbitrary units) for Rayleigh numbers lower and higher than the critical one for the parameter case (c). The unit of time corresponds to 10000 LB integration steps.

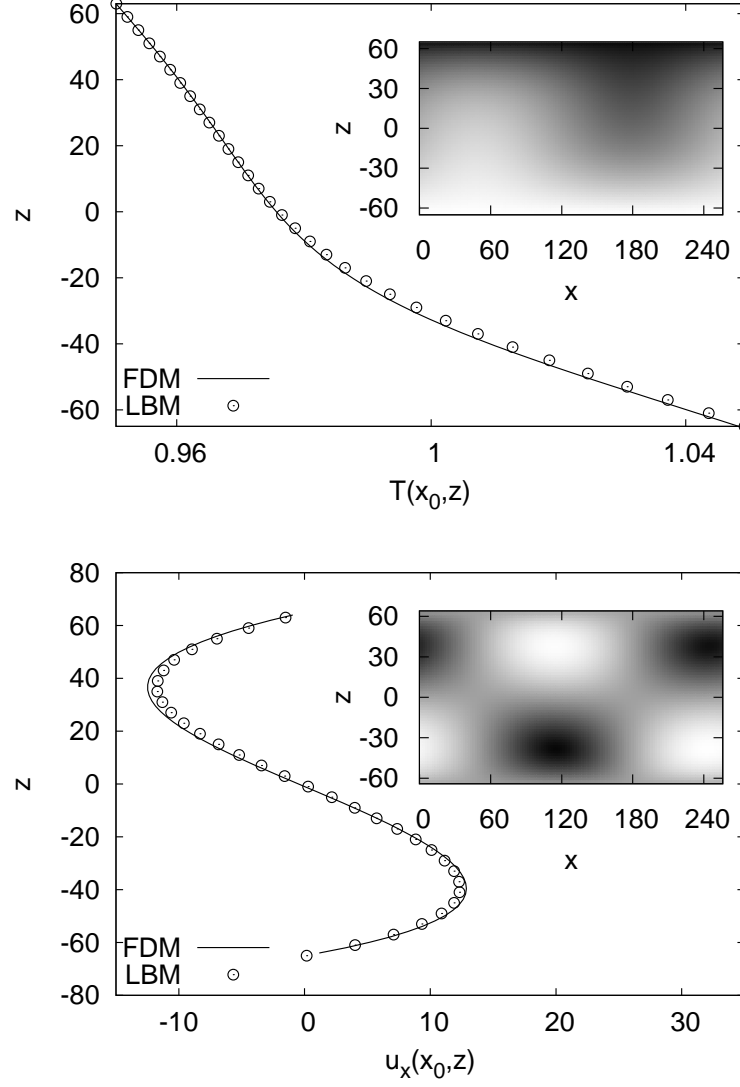


FIG. 3: Comparison between one-dimensional vertical cut of the stationary temperature and velocity profiles after transition to a convective two-rolls configuration. Up: $T(x_0, z)$ at x_0 such that $x_0 = 0.69L_x$. Circles correspond to the Lattice Boltzmann algorithm (LBM); solid line corresponds to a finite difference calculations (FDM) [55, 56]. Down: the same of above plot but for the stream-wise velocity, $u_x(x_0, z)$. In the insets we show a grey-scale coded representations of the convective stationary rolls in the whole two-dimensional domain (up: temperature; down: stream-wise velocity).

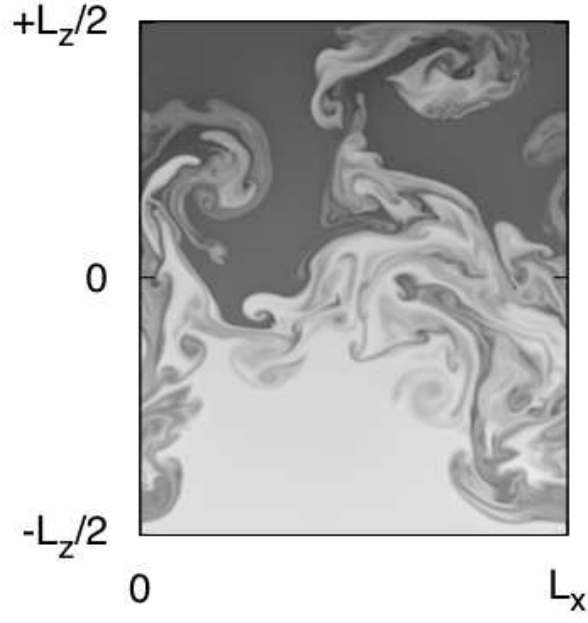


FIG. 4: Spatial configuration for a typical RT run with $L_x \times L_z = 800 \times 2400$, $T_u = 0.95$, $T_d = 1.05$ at time $t = 4\tilde{\tau}$ (run A in table I).

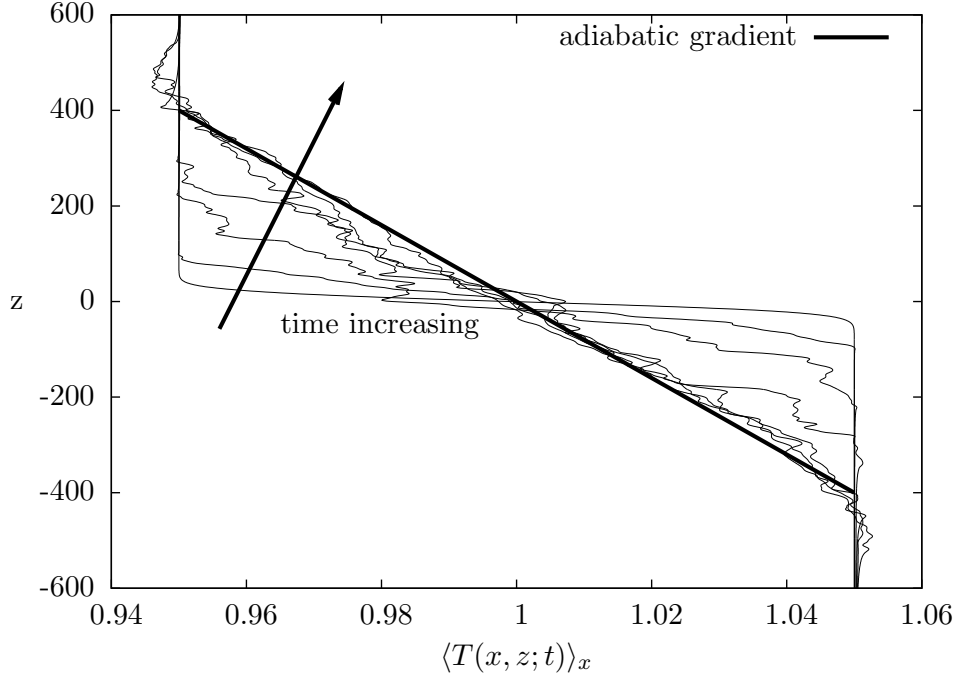


FIG. 5: Temporal evolution of the mean temperature profile, $\langle T(x, z, t) \rangle_x$ at changing time, $t = n\delta t$, with $\delta t \approx 1.5\tau_{ad}$ $n = 1, 2, \dots, 7$. Notice that the profile approaches more and more the linear behaviour dictated by the adiabatic gradient, $\langle T(x, z, t) \rangle_x = (T_u + T_d)/2 - zg/c_p$. Time is adimensionalized by using a reference time based on adiabatic quantities, $\tau_{ad} = \sqrt{L_{ad}/(g \Delta T/T_u)}$

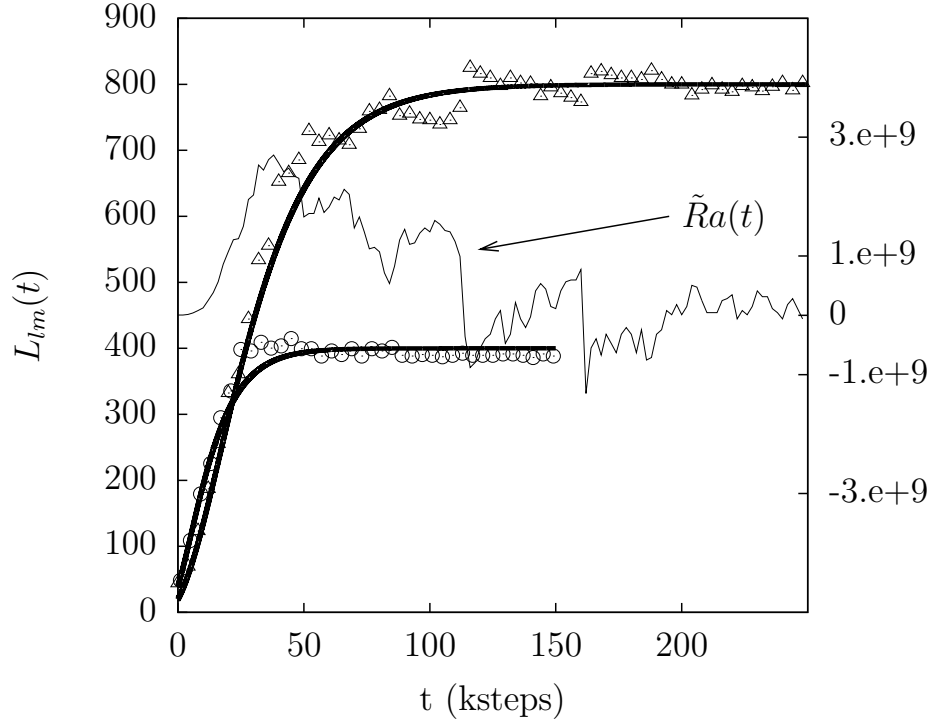


FIG. 6: Evolutions of the mixing layer, $L_{ml}(t)$ versus time with two different adiabatic lengths: (a): $L_{ad} = 800$, $g = 2.5 \cdot 10^{-4}$ (triangles); (b) $L_{ad} = 400$, $g = 5 \cdot 10^{-4}$ (circles); Both cases have $At = 0.05$, $\nu = 0.001$ and $\kappa = 0.002$. Solid bold lines correspond to the theoretical prediction (23) with $\alpha^{(L)} = 0.05$. Continuous line correspond to the evolution of the instantaneous Rayleigh number (20) calculated for case (a), scale on the right y-axis.

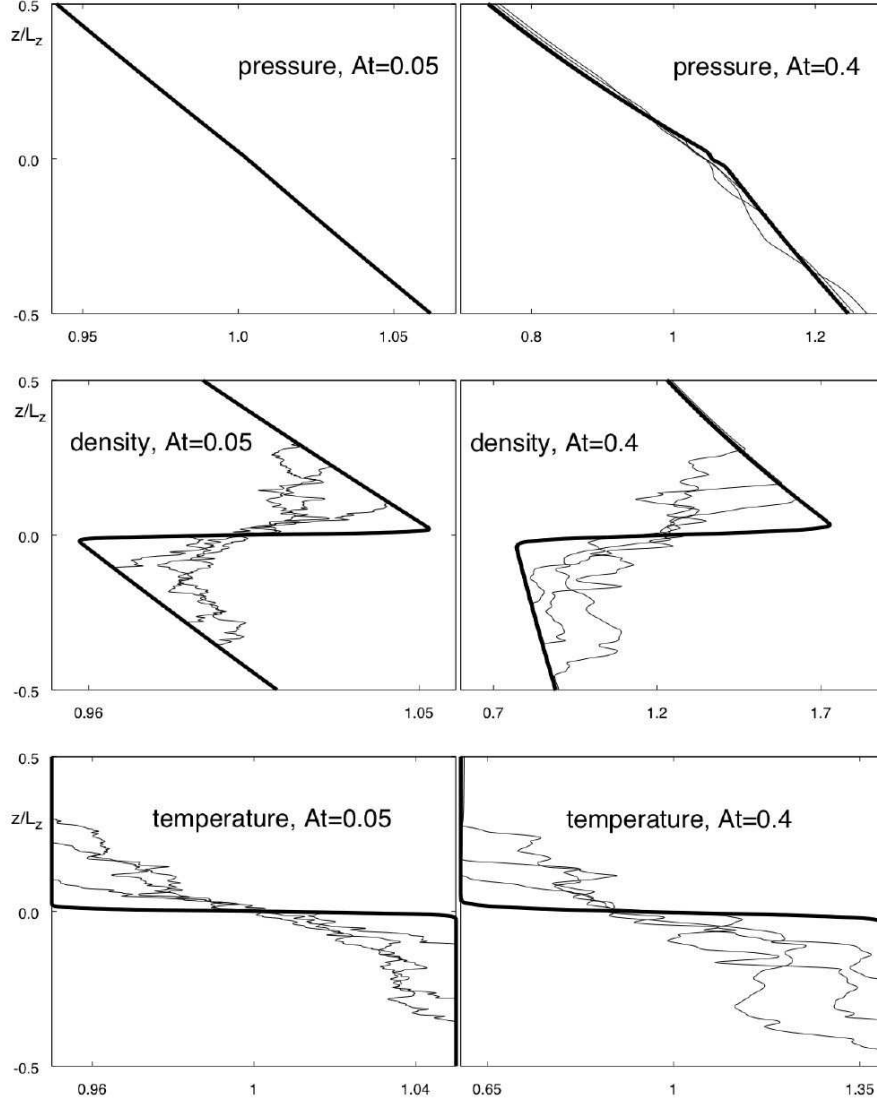


FIG. 7: Temperature, $\langle T(x, z; t) \rangle_x$, density, $\langle \rho(x, z; t) \rangle_x$, and pressure, $\langle p(x, z; t) \rangle_x$, instantaneous mean profiles at different time during the RT evolution. Left column: $At = 0.05$, times $t = 3\tilde{\tau}, 6\tilde{\tau}, 7\tilde{\tau}$ (run A, table I); Right column: $At = 0.4$, times $t = 3\tilde{\tau}, 4.5\tilde{\tau}, 6\tilde{\tau}$ (run B, table I). Initial hydrostatic profiles are depicted by solid bold lines. Notice the asymmetry for the mixing layer growth in the latter case. Notice also the appearance for high Atwood of hydrodynamical pressure fluctuations superposed to the hydrostatic pressure profiles. Both effects are absent in the small Atwood case.

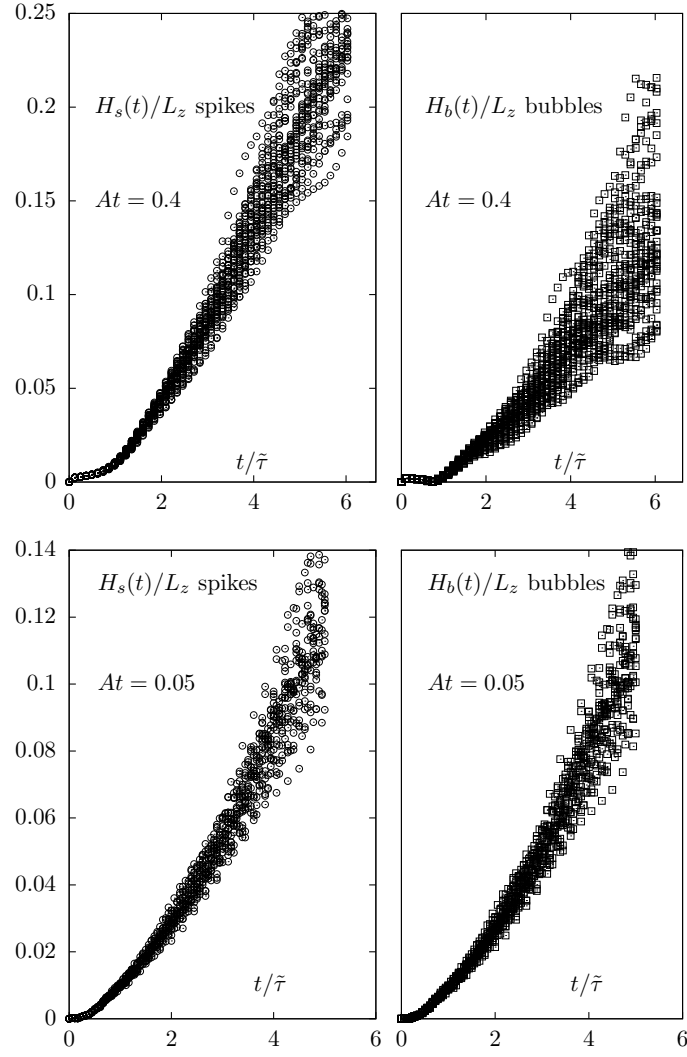


FIG. 8: Growth of $H_{s,b}(t)$, run-by-run, for the two Atwood numbers of run A and run B. The mixing length width is normalized by the total box width, L_z . Notice the evident asymmetry between spikes and bubbles for the high Atwood case (run B).

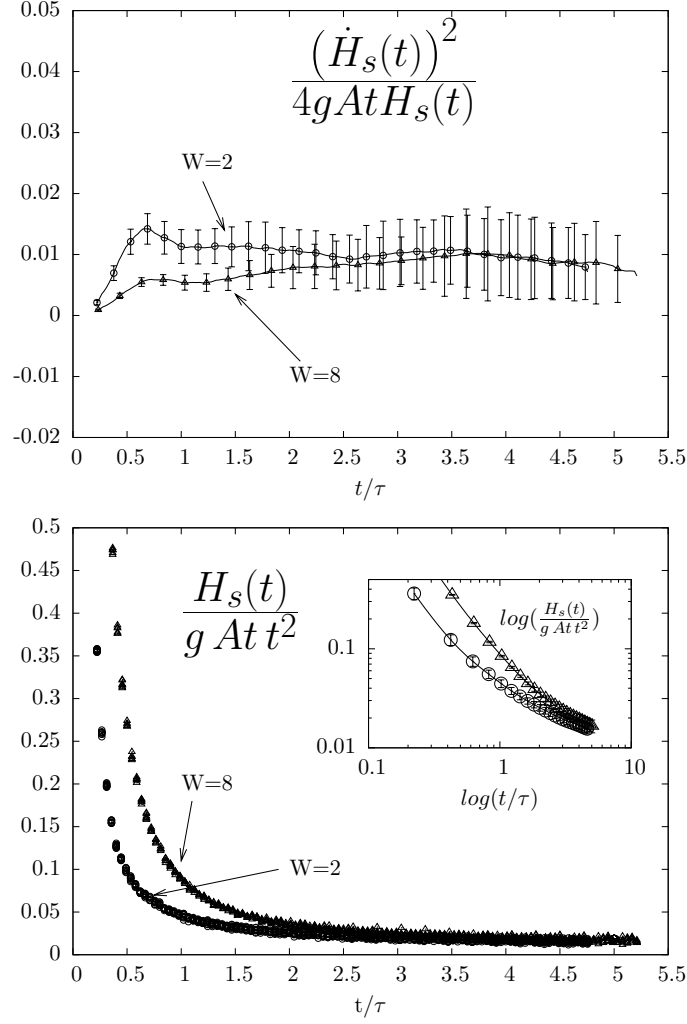


FIG. 9: Run A. $At = 0.05$. Analysis of the asymptotic growth rate for spikes, $\alpha_s^{(H)}$. Bottom panel: mixing length evolution normalized by t^2 for two different set of initial width, $W = \epsilon/\omega = 2$ (circles) and $W = 8$ (triangles), where ϵ is the intensity of the initial perturbation and ω is the width of the regularizing \tanh initial profile. Data refers to $N_{conf} = 50$ for both cases. Notice the long relaxation time before the two evolution forgets the initial conditions. This is due to the presence of the prefactor proportional to $L_{ml}(t_0)$ in the sub-leading linear term of eq. (22). Inset: the mean value of the data shown in the body but in log coordinates -same symbols.

Upper panel: mean value of the instantaneous growth rate of spikes extracted from (30) for the two initial set up with $W = 2, 8$. Average is performed over $N_{conf} = 50$ separate Rayleigh Taylor evolution for the two cases. Error bars are estimated out of root mean square fluctuations. Notice the more extended range where the two set-up superpose and the extended time interval where $\alpha_s^{(H)}$ stays constant (notice the different y-scale between lower and upper panels). Results for bubbles evolution are similar and not shown. Both cases are summarized in figure 10

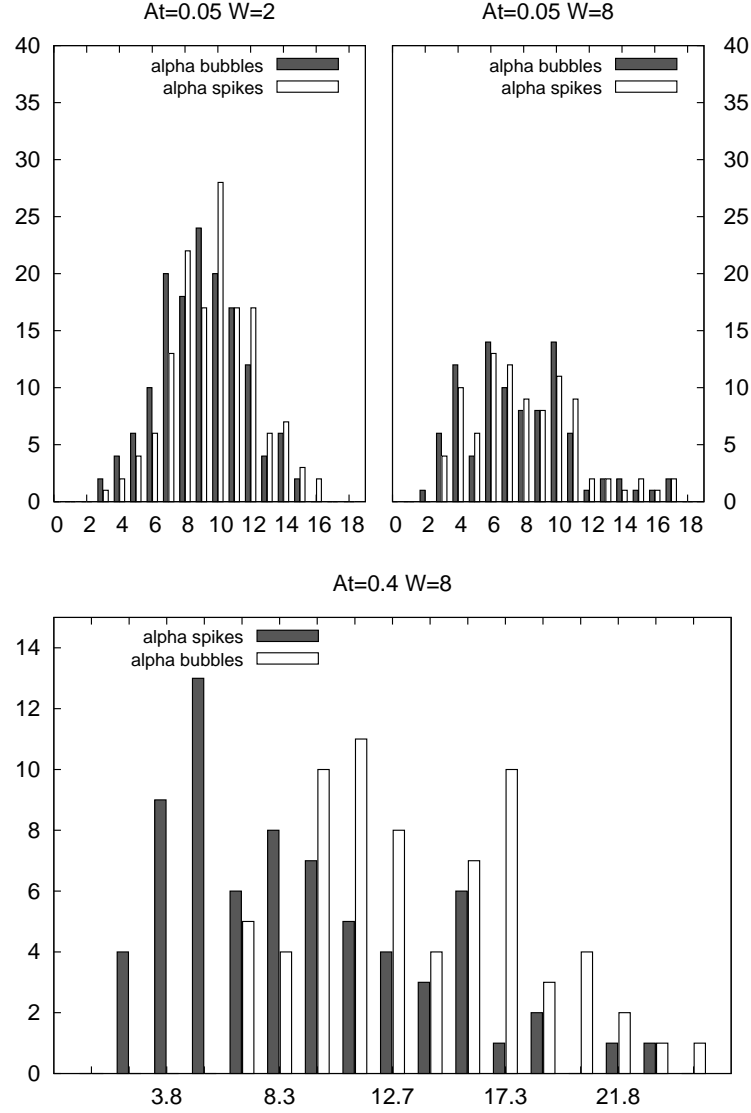


FIG. 10: Top: Run A, $At = 0.05$; histograms of $\alpha_{s,b}^{(H)}$ (multiplied by 10^3 for the sake of clarity) as extracted from (30), at fixed initial width $W = 2$ (left) and $W = 8$ (right). The fit is done over 50 and 35 different configurations respectively. In order to test dependency on the fitting window we have summed results from two different ranges, $t \in [1.5\tilde{\tau} : 4.5\tilde{\tau}]$ and $t \in [2.2\tilde{\tau} : 4\tilde{\tau}]$ in both cases the maximum time is such that the front didn't reach more than 80% of the total vertical extension of the physical domain. Bottom: Run B, $At = 0.4$. Results from two fitting ranges $t \in [2.3\tilde{\tau} : 5.4\tilde{\tau}]$ and $t \in [3\tilde{\tau} : 4.5\tilde{\tau}]$. Notice the asymmetry developing for $At = 0.4$, with spikes traveling faster. An estimate of the mean value for the growth rate in the two cases gives: $\alpha_s^{(H)} = (10 \pm 2) 10^{-3}$ and $\alpha_b^{(H)} = (9.5 \pm 2) 10^{-3}$ at $At = 0.05$, while $\alpha_s^{(H)} = (14 \pm 4) 10^{-3}$ and $\alpha_b^{(H)} = (9 \pm 5) 10^{-3}$ for $At = 0.4$.

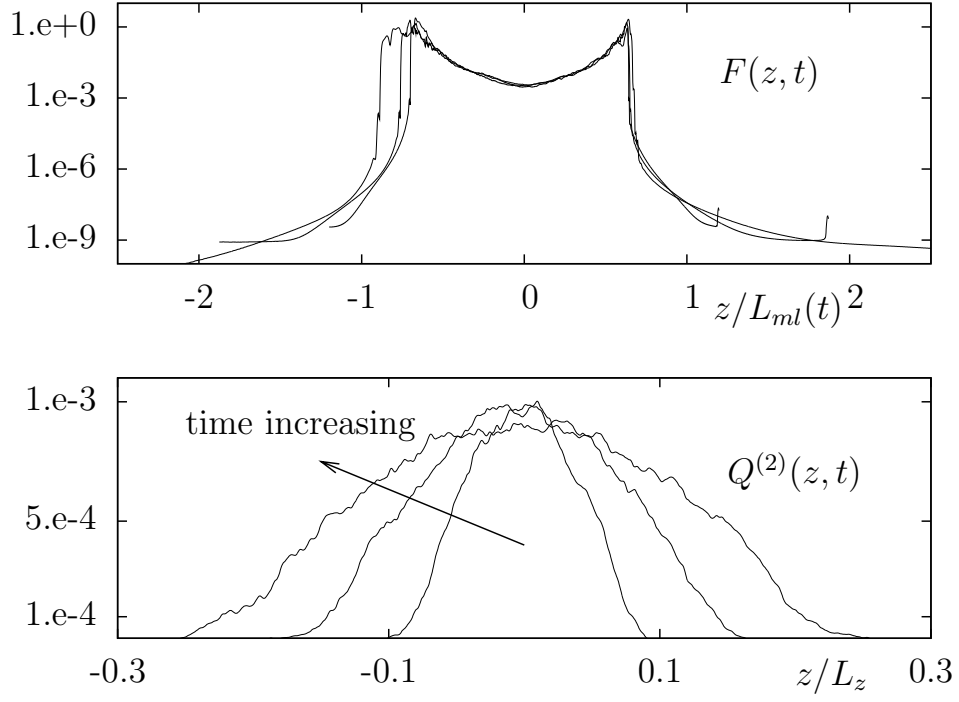


FIG. 11: Bottom: 2nd order moment of temperature fluctuations (see Eqn. (31)) as a function of the height at times $t = (2.2, 3.3, 4.4)\tilde{\tau}$. The z -height has been normalized with the total cell extension L_z . Top: Flatness $Q^{(4)}(z, t)/(Q^{(2)}(z, t))^2$ at the same three instants of time as in the bottom panel. The z -height has been normalized with $L_{ml}(t)$ in order to show the self-similarity of the mixing process (the three curves collapse onto each other by rescaling). Parameters refer to run A in table 1.

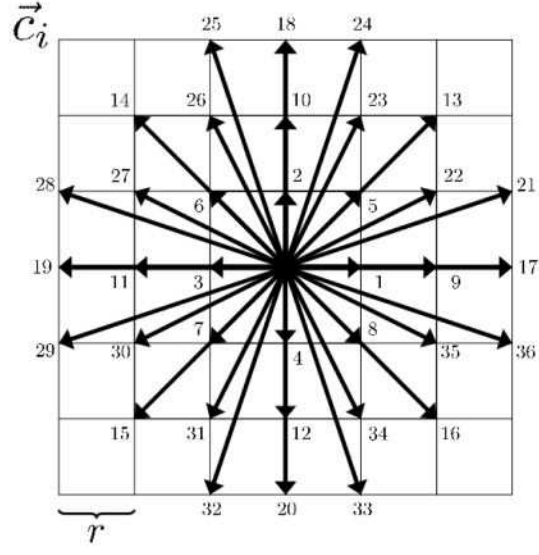


FIG. 12: Scheme for the $D2Q37$ model used for the simulation of thermohydrodynamics. The 'lattice constant' is $r \sim 1.1969$ as reported in [29]. The velocity set is such that every projection of the velocity is an integer multiple of r which is chosen to enforce the unitarity of Hermite polynomials (33,34) up to the fourth order. The relationship between real and velocity lattice is set by $\Delta x = r\Delta t$ with Δx and Δt space and time discretizations. Based on the Hermite-Gauss quadrature procedure [15, 26, 29], the $D2Q37$ can be regarded as the minimal on grid square lattice giving with accurate Hermite polynomials up to the fourth order. This quadrature ensures that the Navier-Stokes thermodynamics is recovered with full Galilean invariance. Lattice $D2V37$ firstly appeared and was shown to be minimal for $2d$ fourth order models in Reference [26], where the authors formally showed the equivalence between the condition of norm preservation and the preservation of the orthogonality property, in constructing these sets of lattice vectors.

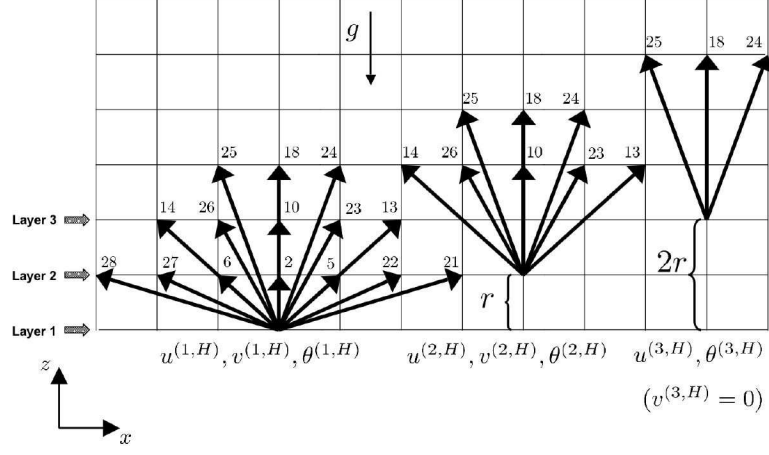


FIG. 13: Scheme for the lower boundary layer for the simulation of thermal flows under the effect of gravity. The relationship between real and velocity lattice is set by $\Delta x = r\Delta t$ with Δx and Δt space and time discretizations, and r the lattice constant whose value is $r \sim 1.1969$. the locations at r and $2r$ indicated in this figure correspond to the locations $z = 2$ and $z = 3$ discussed in the text.